Two-dimensional perovskite materials: From synthesis to energy-related applications

Changyong Lan [a, b], Ziyao Zhou [a, c], Renjie Wei [a, c], Johnny C. Ho [a, c, d, *]

[a] Department of Materials Science and Engineering, City University of Hong Kong, Hong Kong, China
[b] School of Optoelectronic Science and Engineering, University of Electronic Science and Technology of China, Chengdu 610054, China
[c] Shenzhen Research Institute, City University of Hong Kong, Shenzhen 518057, China
[d] Centre of Functional Photonics, City University of Hong Kong, Hong Kong, China

ARTICLE INFO

ABSTRACT

Due to the superior optoelectronic properties of halide perovskites, it has attracted wide attentions during the past decade, especially in the field of energy. When the dimension of halide perovskites reduces, novel properties will appear, such as large exciton binding energy, high photoluminescence quantum yield, and enlarged band gap. This way, low dimensional halide perovskites, especially two-dimensional (2D) halide perovskites, have attracted intensive attention in recent years and showed promising applications, including photodetectors, light emitting diodes (LEDs), and solar cells. Various methods were then developed for the synthesis of 2D halide perovskites and studying the exciting optoelectronic properties. The optoelectronic devices based on 2D halide perovskites showed excellent performance, particularly high sensitive photodetection, high electroluminescence with sharp emission peak, and environmental stable solar cells with decent power conversion efficiency. In this case, 2D halide perovskites become superstar materials in perovskites research area. In this review, we summarize the recent progresses in the synthesis and energy applications of 2D halide perovskites, and challenges and future directions in the field.

© 2018 Elsevier Ltd. All rights reserved.

1. Introduction

In the past decade, perovskite materials, especially the organic—inorganic mixed halides, have attracted wide attention for energy-related applications due to their superior electrical and optoelectronic properties. Since the first report of the utilization of methylammonium ($CH_3NH_3^+$, MA^+) lead halide perovskite ($MAPbI_3$) in solar cells by Kojima et al. in 2009 [1], the power conversion efficiency (PCE) of halide perovskite based solar cells exceeded over 20% in just a few years of rapid research and development [2], which evidently indicated the technological potency of mixed halide perovskites as active materials for the photovoltaics as compared with other conventional semiconductors. In general, the high PCE of mixed halide perovskites originates from their excellent absorption coefficients with suitable band gaps [3,4], outstanding carrier mobilities [5–7], long carrier diffusion lengths [8–13], low

trap densities [11], and low exciton binding energies [14,15], etc. Also, there are some other remarkable features, such as the intense photoluminescence (PL), rich phase compositions, good stoichiometric and property tenability, low-temperature solution processability and so on, which have been lately discovered with these perovskite materials [16]. In this regard, in addition to high-efficiency solar cells, all these impressive properties of halide perovskites [17] can as well make them suitable for other energy-related applications, including low-power transistors [18–20], highly-efficient photodetectors [21–24], and light emitting diodes (LEDs) [25–27]. With all these extensive application opportunities, the mixed halide perovskites have become a superstar in materials science and several other scientific communities.

At the same time, there are significant amounts of recent works focused on the two-dimensional (2D) perovskite materials because of their unique physical and chemical properties arising from the quantum confinement effect [28,29]. For example, when the dimension of perovskites is reduced to 2D, many of their exotic characteristics would start to appear, together with the much enhanced stability in ambient, substantially extending them to wider application domains [30–34]. One way to obtain the 2D

* Corresponding author. Department of Materials Science and Engineering, City University of Hong Kong, Hong Kong, China.
E-mail address: johnnyho@cityu.edu.hk (J.C. Ho).

perovskites is simply to thin down the thickness of three-dimensional (3D) perovskites into atomically thin films, where this fabrication approach has been successfully realized by various kinds of synthesis methods till now. Among many 2D perovskites obtained by different techniques, there is a special kind of perovskites, known as Ruddlesden–Popper (RP) perovskites, which are similar with conventional 2D materials having a van der Waals layered crystal structure [35]. Interestingly, this particular kind of perovskites have the naturally integrated quantum well structures exhibiting quantum confinement effects without physically thinning down to the atomic thickness, which are in a distinct difference to the typical layered materials. As a result, these perovskites are also named as 2D or quasi-2D perovskites [34–37]. In any case, owing to their improved environmental stabilities, large exciton binding energies, high quantum yields and other rich photophysics properties, these RP 2D perovskites also find themselves as promising candidates for next-generation energy-efficient optoelectronics.

In this review, we aim to highlight the recent advancements in the synthesis, assessment of optoelectronic properties, and energy-related applications of 2D perovskites, including both conventional 2D perovskites and RP perovskites. In specific, this work is divided into five sessions. First, the crystal structures of halide perovskites are introduced, spanning all the way from 3D mixed halide perovskites to RP halide perovskites. Second, the recent progresses in the synthesis of 2D halide perovskites are presented. Third, the intriguing optoelectronic properties of 2D halide perovskites, especially the RP perovskites, are introduced. Fourth, the recent achievements in energy-related applications of 2D halide perovskites are also surveyed. Eventually, an outlook of the future development of 2D halide perovskites is also given, which may serve as important guidelines for the optimal design of 2D perovskites for various technological applications.

2. Crystal structures of halide perovskites

Typically, 3D halide perovskite materials have a cubic crystal structure similar to $CaTiO_3$, which can be written in the form of ABX_3 as schematically shown in Fig. 1a. A and B are cations, and X represents an anion. In explicit, A cations locate at the interstices of the corner-sharing BX_6 octahedral network, forming the structure of 3D perovskites. For maintaining a stable ABX_3 structure, the Goldschmidt tolerance factor (t) of the perovskite should be close to 1, in which it is always within a range of between 0.813 and 1.070. The Goldschmidt tolerance factor is defined as $t = (R_A + R_B)/[\sqrt{2}(R_X + R_B)]$, where R_A, R_B, and R_X are the ionic radii of the corresponding ions of A, B and X, respectively [38]. For halide

perovskites, A sites are occupied by the ions of Cs^+, MA^+, or formamidinium ($NH_2CHNH_2^+$, FA^+), B sites are taken by the ions of Pb^{2+} or Sn^{2+}, and X sites are engaged with the halide anions, such as Cl^{-1}, Br^{-1}, and I^{-1}. It is also noted when A sites are occupied by the groups that are too large, such as the long-chain alkyl amine cations, the lead halide perovskites would turn into the above-discussed 2D layered structure (e.g. RP perovskites) as illustrated in Fig. 1b and c.

For RP perovskites, the general chemical formula is written as $L_2A_{n-1}B_nX_{3n+1}$, where L^+ is the long chain molecular cation, such as aliphatic and aromatic alkylammonium cations. Importantly, this organic cation L^+ must contain terminal functional groups, which can ionically interact with the anionic inorganic substructure but without reacting with the rest of organic molecules, being stable with the inorganic components B and X [39]. The most common long chain molecular cations of 2D RP perovskites are n-butylammonium (n-BA) and 2-phenylethylammonium (PEA). More detailed information about the other long chain molecular cations can be found in the literature [35]. As demonstrated in Fig. 1b and c, the BX_6 perovskite sublayer is sandwiched by the long chain molecular cations. The value of n determines the number of BX_6 octahedrons along the sandwiched direction. Since the long chain molecular cations are always insulating, the sandwiched structure would behave like a multiple quantum well structure, where the inorganic slabs serve as the well while the organic layers function as the potential barriers. Due to the strictly periodical spatial arrangement of the metal halide structures as well as the packing of the organic species around them, RP perovskites can be considered as the bulk assemblies of 2D quantum wells. The isolation of the interior metal halide sublayers sandwiched by the wide band gap organic ligands can effectively inhibit interactions between metal halide layers, which allows the bulk crystals to exhibit the intrinsic properties of individual metal halide layers [40]. This phenomenon is totally different from the conventional layered materials, including WS_2 and graphite, where the individual layer shows very different properties as compared with their bulk counterparts. This way, these RP layered perovskites can also be called 2D perovskites or quasi-2D perovskites depending on the layer numbers of BX_6 units stacked along the sandwiched direction. When the n value is greater than 4, the terminology of quasi-2D perovskites is commonly referred. In this report, in order to differentiate these quasi-2D perovskites from the typical 2D perovskites fabricated by thinning down 3D perovskites to the atomic thickness, this particular kind of 2D perovskites are named as 2D RP perovskites in the following sessions.

3. Synthesis of 2D perovskites

Controllable synthesis of 2D perovskites is important for the investigation of their fundamental properties and device applications. Till now, various kinds of atomically thin perovskites have been synthesized using different kinds of techniques. In this session, we will discuss the recent progresses in the synthesis of 2D perovskites. As the halide perovskites can be categorized into organic–inorganic mixed halide perovskites, 2D RP perovskites, and inorganic halide perovskites, the following discussion will be divided into three subparts according to the classification.

3.1. Organic–inorganic mixed halide perovskites

Since $MAPbX_3$ (X = Cl, Br, I) is a non-layered 3D perovskite material, it is relatively difficult to obtain 2D perovskites directly from their 3D counterparts, especially by the universal scotch tap based mechanical exfoliation method utilized in obtaining conventional 2D materials, such as graphene, and MoS_2, etc. [41].
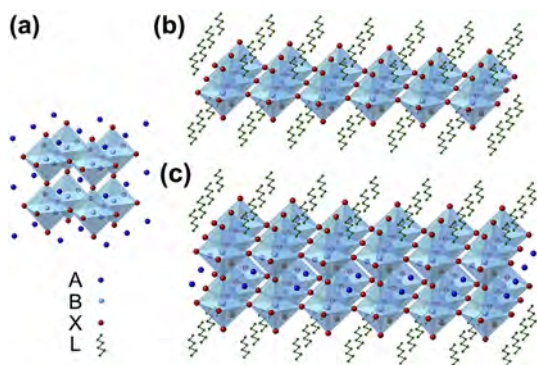

Fig. 1. Illustrative schematic of the crystal structure of different halide perovskite materials. (a) Perovskites with the chemical formula ABX_3. (b) RP perovskites with $n = 1$. (c) RP perovskite with $n = 2$. The chemical formula of RP perovskites is $L_2A_{n-1}B_nX_{3n+1}$.

Fortunately, one of the precursors for synthesizing MAPbX₃ perovskites, PbX₂, has a van der Waals layered crystal structure. This way, it is possible to first obtain the atomically thin PbI₂ flakes, which can then be chemically transformed into MAPbX₃. In general, chemical vapor deposition (CVD) technique is a convenient way for the growth of atomically thin PbI₂ nanoplatelets [42]; therefore, CVD combined with the subsequent chemical conversion is widely used for the synthesis of MAPbX₃ nanoplatelets. For instance, Ha et al. have synthesized halide perovskite nanoplatelets using the two-step CVD method [43]. At first, PbI₂ nano-platelets were epitaxially grown on muscovite mica substrates via vapor transport CVD; next, the as-grown PbI₂ nanoplatelets were converted to perovskites by reacting with methylammonium halide (MAI) gases in a CVD chamber as shown in Fig. 2a. The prepared perovskite nanoplatelets typically exhibited a lateral domain size of 5−30 μm. Due to the insertion of the organic molecules in PbI₂, the thickness of the resulting perovskite nano-platelets were found to increase slightly as compared with that of PbI₂ as illustrated in Fig. 2b. A linear relation between the thickness of PbI₂ and MAPbI₃ nano-platelets could be obtained following the equation of $t_{MAPbI_3} = 1.81 t_{PbI_2} - 2.2$. Other perovskite nano-platelets, such as MAPbBr₃, MAPbCl₃, MAPbI$_x$Cl$_{3-x}$, and MAPbI$_x$Br$_{3-x}$, could also be synthesized by the similar method with different lead halide and methyl-ammonium halide sources [43]. However, the thickness of the obtained perovskite nanoplatelets was still relatively thick, being on the order of tens to hundreds of nanometers. By further optimizing the evaporation temperature of PbI₂, substrate temperature, and deposition time, Niu et al. could obtain PbI₂ platelets with the controlled thickness on Si/SiO₂, which could be consequently converted into MAPbI₃ platelets [44]. The thickness of resulting MAPbI₃ nanoplatelets could be reliably controlled from few layers to hundreds of nanometers. Apart from usual 2D growth on smooth underlying substrates, as the morphology of PbI₂ can be well tuned

by CVD method, Lan et al. recently developed a method to achieve the synthesis of free-standing PbI₂ nanosheets utilizing the surface micro-environment of the roughened substrate and then converted them into free-standing MAPbI₃ nanosheets [22].

Ultra-thin PbI₂ nanoflakes could also be obtained by solution based methods because of their layered structure. This way, atomically thin MAPbI₃ flakes were able to be achieved by the chemical conversion of ultra-thin PbI₂ flakes from solution method [45]. In particular, atomically thin PbI₂ flakes could be synthesized by casting the saturated aqueous PbI₂ solution onto a substrate and successively heating the processed substrate at an elevated temperature. After that, the atomically thin PbI₂ flakes were converted into MAPbI₃ flakes in a CVD system. The synthesis process is also depicted in Fig. 2c. It was found that the heating temperature of this solution process was crucial in order to control the nucleation and growth of 2D PbI₂ nanosheets since the number of nucleation sites was predominantly controlled by temperature. By utilizing this method, MAPbI₃ flakes with the thickness of 1-, 2-, 4-, and 10-layer were successively obtained (Fig. 2d). Furthermore, Wang et al. developed another method for the synthesis of MAPbI₃ microplate arrays as schematically presented in Fig. 2e [46]. In detail, the SiO₂/Si substrate was first functionalized with self-assembled monolayers of (octadecyl)tri-chlorosilane (OTS) to yield a hydrophobic surface and then lith-ographically patterned to create periodic arrays of hydrophilic areas. A hot aqueous PbI₂ solution was used as a seeding solution to produce PbI₂ seed particles in hydrophilic regions using a flow seeding process. The seeded substrate was next immersed in a saturated PbI₂ solution at 80 °C to further grow the seeds into larger PbI₂ microplates. Eventually, the as-grown PbI₂ flakes could be chemically converted into MAPbI₃ microplates. This method is extremely useful for the fabrication of perovskites based device arrays owing to its versatility.
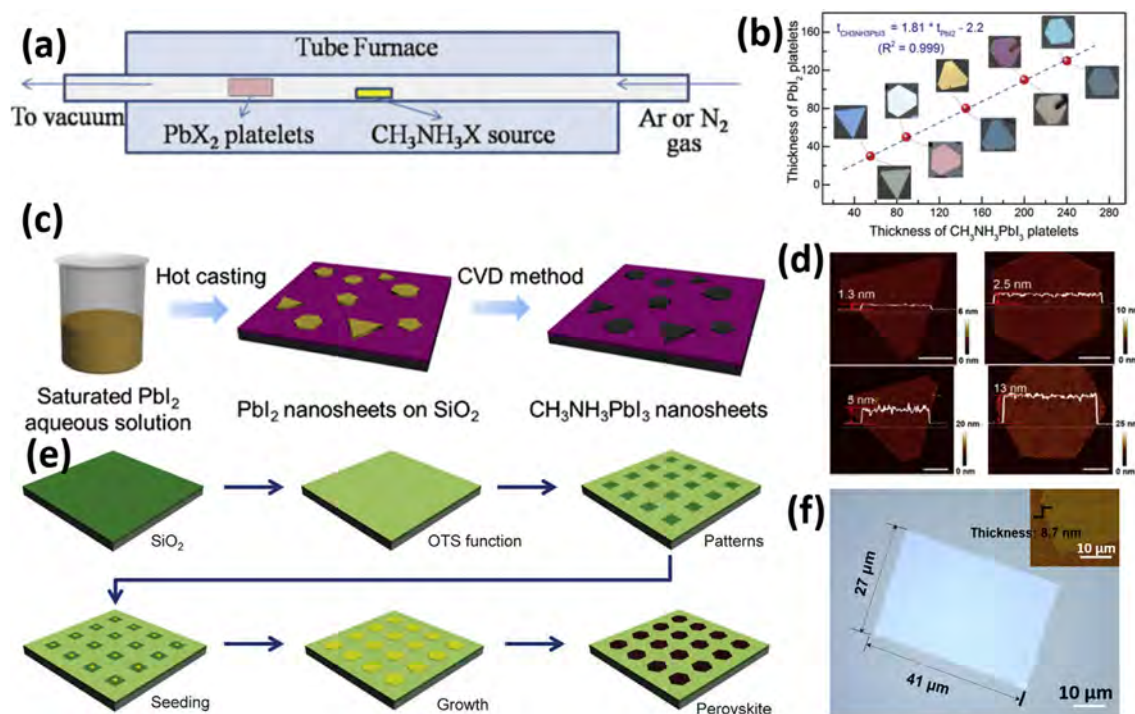

Fig. 2. Synthesis of organic−inorganic mixed halide perovskites. (a) Experimental setup for the conversion of PbX₂ into MAPbX₃. (b) Thickness of PbI₂ platelets before and after being converted to MAPbI₃ platelets. (a), (b) Reproduced with permission from Ref. [42]. Copyright 2014, WILEY-VCH. (c) Illustrative schematic for the synthesis of MAPbI₃ nanosheets by hot casting method. (d) AFM images of the MAPbI₃ nanosheets. (c), (d) Reproduced with permission from Ref. [44]. Copyright 2016, American Chemical Society. (e) Illustrative schematic for the synthesis of perovskite microplates arrays. Reproduced with permission from Ref. [45]. Copyright 2015, American Association for the Advancement of Science. (f) Optical microscopy image and AFM image (inset) of a MAPbCl₃ nanosheet. Reproduced with permission from Ref. [46]. Copyright 2015, American Chemical Society.

Moreover, direct CVD method together with van der Waals epitaxy were employed to synthesize MAPbCl$_3$ nanosheets with the large lateral domain size up to tens of micrometers and the thickness down to several nanometers (Fig. 2f) [47]. Specifically, PbCl$_2$ and MACl powders were used as the precursor sources, while muscovite mica substrates were selected for the van der Waals growth of MAPbCl$_3$. The reaction was performed in a horizontal tube furnace at a pressure of 120−160 Torr. The source and growth temperatures were carefully designed to control the deposition. During the growth, PbCl$_2$ powders were placed in the center of the furnace with a temperature of 360 °C, MACl powders were placed upstream with a relatively low temperature of 200 °C, and the muscovite mica substrate was placed downstream with a temperature of 200 °C. This way, square-shaped perovskite nanosheets with the lateral domain size of tens of micrometers could be prepared. From Monte Carlo simulations, they found that the competition between the van der Waals diffusion and surface free energy of the perovskite would lead to film thickening. As a result, in order to achieve the atomically thin MAPbI$_3$ flakes by direct CVD, surface passivation is essential to reduce the film thickening effect here.

3.2. 2D RP perovskites

Due to the van der Waals layered crystal structure of 2D RP perovskites, it is quite straight-forward to obtain atomically thin layers of perovskites by mechanical exfoliation similar to the cases in conventional 2D materials, such as graphene [41]. By using micromechanical exfoliation technique, Niu et al. could ultimately obtain one-layer to several layers of (C$_6$H$_9$C$_2$H$_4$NH$_3$)$_2$PbI$_4$ flakes as shown in Fig. 3a [48]. This synthesis method is extremely suitable to get hold of ultrathin flakes for studying the basic properties of quasi-2D perovskites with different layer numbers [49,50], but it cannot be used for practical material manufacturing because of the lack of size and thickness control of the obtain flakes. Thus, other methods were developed for the synthesis of atomically thin 2D RP perovskites. Dou et al. have successfully synthesized atomically thin BA$_2$PbBr$_4$ perovskite (BA = C$_4$H$_9$NH$_3^+$) by solution based method [51]. Using ultra-low concentration of the mixture of BABr and PbBr$_2$ (molar ratio of 2:1) in the ternary organic solvent (e.g. chlorobenzene-dimethylformide-acetonitrile) and controlling the evaporation temperature, monolayer and few-layer BA$_2$PbBr$_4$ perovskite nanosheets could be obtained on the Si/SiO$_2$ substrate.

This particular method could be further extended to the synthesis of ultrathin BA$_2$PbCl$_4$, BA$_2$PbI$_4$, BA$_2$PbCl$_2$Br$_2$, BA$_2$PbBr$_2$I$_2$, and BA$_2$MAPb$_2$Br$_7$ 2D nanosheets by simply using different precursors [51]. At the same time, Chen et al. carried out a systematical investigation on this method and found the critical factors affecting the growth of 2D perovskites, which were the solvent volume ratio, crystallization temperature, and solvent polarity [52]. Under the optimal reaction condition, 2D BA$_2$PbBr$_4$ perovskites with the largest lateral dimension of 40 μm and the smallest thickness of down to a few nanometers were obtained (Fig. 3b). Furthermore, the same research group also developed a self-doping engineering method for the synthesis of ultrathin and large size 2D homologous BA$_2$MA$_{n-1}$Pb$_n$Br$_{3n+1}$ perovskites using 2D BA$_2$PbBr$_4$ nanosheets as the template with MA$^+$ dopants (Fig. 3c) [53]. In explicit, 2D BA$_2$PbBr$_4$ nanosheets were first synthesized by a solvent-based method. Next, the 2D BA$_2$PbBr$_4$ nanosheets were transformed into 2D homologous BA$_2$MA$_{n-1}$Pb$_n$Br$_{3n+1}$ perovskites by CVD at 120 °C for 30 min. The self-doping of 2D perovskites could yield BA$_2$MA$_{n-1}$Pb$_n$Br$_{3n+1}$ with different n values from 2 to ∞ depending on the self-doping time. This way, ultrathin BA$_2$MA$_{n-1}$Pb$_n$Br$_{3n+1}$ perovskites were able to be formed via an intercalation mechanism with the thickness shrinking down to 4.2 nm and the lateral dimension up to 57 μm. Zhang et al., on the other hand, used a binary mixture of solvents as the perovskite precursors [54]. Acetonitrile is an appropriate solvent for the precursors while toluene is a poor solvent that is known to induce the precipitation of perovskite crystals. Here, these two solvents are perfectly miscible, which could slowly coevaporate at room temperature, allowing the controlled synthesis of 2D RP perovskites on substrates. As a result, PEA$_2$PbI$_4$, BA$_2$PbI$_4$, (C$_6$H$_{13}$NH$_3$)$_2$PbI$_4$, (C$_{12}$H$_{25}$NH$_3$)$_2$PbI$_4$, and (C$_{16}$H$_{33}$NH$_3$)$_2$PbI$_4$ nanosheets with different thicknesses were successfully obtained.

Although these 2D RP perovskites with large lateral size have been synthesized, these nanosheets were all obtained on substrates, in which complex techniques were required in order to transfer all those nanosheets to other substrates, restricting their further device applications. Alternatively, colloidal-based methods were explored for the synthesis of 2D RP perovskite nanosheets. Yang et al. developed a more controllable scheme to grow single- and few-layer free-standing PEA$_2$PbX$_4$ (PEA = C$_8$H$_9$NH$_3^+$, X = C, Br, I) with the uniform lateral size [55]. In particular, PEAI and PbI$_2$ with molar ratio of 2:1 were dissolved in N,N-dimethylformamide
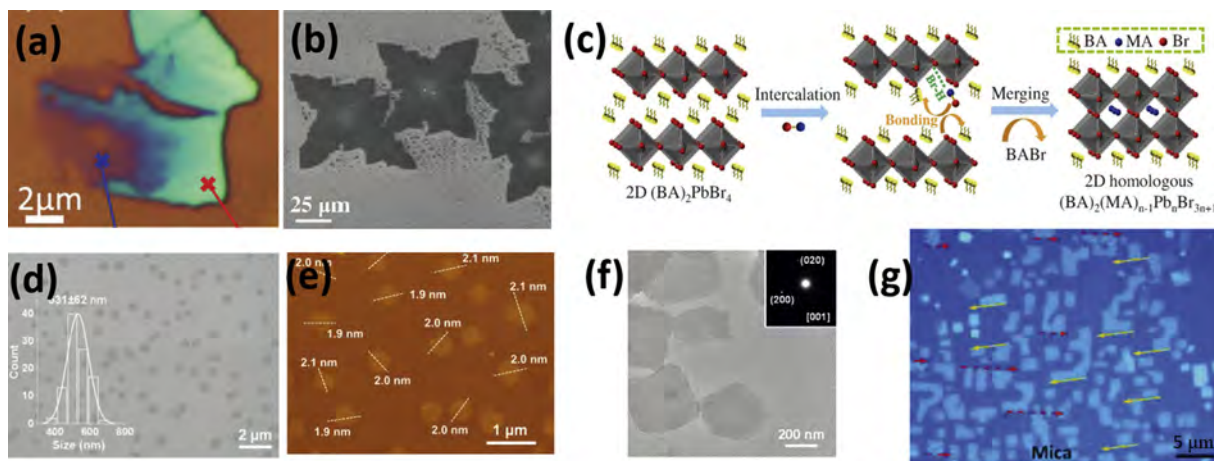

Fig. 3. Synthesis of 2D RP perovskites. (a) Optical microscopy image of (C$_6$H$_9$C$_2$H$_4$NH$_3$)$_2$PbI$_4$ flakes obtained by micromechanical exfoliation technique. Reproduced with permission from Ref. [47]. Copyright 2014, AIP Publishing. (b) SEM image of BA$_2$PbBr$_4$ perovskite nanosheets obtained by solution based method. Reproduced with permission from Ref. [51]. Copyright 2017, WILEY-VCH. (c) Illustrative schematic of self-doping engineering method for 2D RP perovskites. Reproduced with permission from Ref. [52]. Copyright 2017, WILEY-VCH. (d) TEM image of PEA$_2$PbX$_4$ nanosheets. (e) AFM image of PEA$_2$PbX$_4$ nanosheets. (f) TEM image of PEA$_2$PbX$_4$ nanosheets. (d)–(f) Reproduced with permission from Ref. [54]. Copyright 2017, WILEY-VCH. (g) Optical microscopy image of BA$_2$PbI$_4$ flakes. Reproduced with permission from Ref. [57]. Copyright 2017, WILEY-VCH.

(DMF), and the solution was then quickly dropped into toluene under vigorous stirring at room temperature. After 10 min, the perovskite nanocrystals were formed with the lateral size of 531 ± 62 nm and thickness of 2.0 ± 0.1 nm (Fig. 3d–f). By substituting toluene with other solvents, such as chlorobenzene, chloroform, and dichloromethane, the lateral size of the perovskite nanocrystals can be better controlled.

In any case, despite solution-based methods have received considerable achievement, the crystal quality of obtained flakes is still relatively low as compared with the mechanical exfoliated ones. Since CVD is widely used for the synthesis of conventional 2D materials, such as MoS_2 [56], and WS_2 [57], in which this popular technique can also be utilized to grow atomically thin 2D RP perovskites. For example, high-quality and atomically thin BA_2PbI_4 flakes with the lateral size of 5–10 μm and rectangular shape were readily grown on mica substrates via van der Waals epitaxy using CVD method (Fig. 3g) [58]. It should be noted that the layered structure of 2D perovskites actually complicated the growth of thin 2D perovskites. On the one hand, large organic ligands have the very low mobility, and hence, it is hard for BA_2PbI_4 molecules to migrate on the substrate surface, which makes the easy formation of clusters rather than flakes. On the other hand, the vapor pressure of PbI_2 is several orders lower in magnitude than that of the organic ligands of $C_4H_9NH_2$ due to the higher melting point of the former one. This way, these two components tend to condense in different areas after being carried to the downstream, in which most of PbI_2 would have been consumed during cooling with only few left to react with BAI. In order to overcome those limitations obtaining the 2D flakes, the temperature gradient in the downstream area was increased by using a narrow heating belt. Simultaneously, the heating temperature of PbI_2 was reduced slightly to reduce the reaction rate. In this case, BA_2PbI_4 flakes with the well-defined thickness could be reliably obtained.

In addition, liquid exfoliation was also exploited to synthesize 2D RP perovskites from 3D perovskites by inserting the long chain molecules into the 3D perovskite structures. Hintermayr et al. reported the synthesis of $OlA_2MA_{n-1}Pb_nX_{3n+1}$, where OlA was oleylamine cation ($C_9H_{18}=C_9H_{17}NH_3^+$), and X was Cl, Br, or I [59]. During the process, $MAPbX_3$ microcrystal powder was first dispersed in toluene together with OlA and subjected to tip sonication. Then, by centrifugation, the large particles were removed and the nanoplate dispersion was achieved. Interestingly, this method simply relied on the use of solvents, which can effectively reduce the energy of exfoliation according to the Hansen solubility parameter optimization. In this case, the ligand OlA would assist in the exfoliation, protecting the obtained nanoplates from agglomeration and rendering them dispersible in the organic solvents.

3.3. Inorganic halide perovskites

For inorganic halide perovskites, colloidal synthesis method is the most widely used technique for obtaining 2D perovskites [60–64]. Bekenstein et al. synthesized $CsPbBr_3$ nanoplates by injecting Cs-oleate solution into $PbBr_2$ solution with mixed solvent (i.e. mixture of octadecene, oleic acid, and oleylamine) at elevated temperatures [61]. The reaction temperature was found to play a critical role in determining the shape and thickness of resulting nanoplates. Reactions conducted at 150 °C would produce mostly nanocubes, while nanoplates could be obtained at the relatively lower temperatures. For instance, nanoplates with the lateral dimension of 20 nm and the thickness of ~3 nm could be attained at 130 °C. Moreover, $CsPbI_3$ and $CsPbCl_3$ nanoplates could be grown through anion exchange and these nanoplates can be coated onto substrates by centrifugal casting method for device

applications [63]. However, the lateral size is only about 20–300 nm (Fig. 4a), which is not large enough for the evaluation of fundamental properties of individual nanosheet and/or corresponding device fabrication. Shamsi et al. found that $CsPbBr_3$ ultra-thin sheets (3 nm) with the rectangular shape and the controlled lateral size from 300 nm to 5 μm could be obtained by using oleic acid to dissolve Cs-oleate and introducing short ligands (Fig. 4b) [64]. The use of oleic acid as a solvent for Cs-oleate would lead to the formation of nanoplates in a wide range temperatures, spanning from 50 to 150 °C. The drawback is that the lateral size could only be controlled from 50 to 200 nm with the simultaneous increase of thickness. In order to get nanoplates with the large lateral dimension, shorter ligands, octanoic acid and octylamine could be introduced into the solution. By varying the ratio of the two short ligands over that of the longer ligands (e.g. oleic acid and oleylamine), the lateral size of nanoplates could be well controlled from 300 nm to 5 μm, while the thickness of nanoplates was confined to only 2–3 unit cells (i.e. 2.5–3 nm thick).

Moreover, CVD was also explored to grow various inorganic lead perovskites. Zhang et al. have employed van der Waals epitaxial CVD method using mica as substrates for the synthesis of $CsPbX_3$ (X = Cl, Br, I) nanoplatelets [65]. The nanoplatelets had square shapes, which was originated from the intrinsic cubic phase of perovskites. The square nanoplatelets were well oriented at multiples of 90°, suggest the epitaxial nature of the nanoplates on mica as shown in Fig. 4c. Even though the lateral dimensional of the perovskite nanoplatelets was quite large in the range of 1–20 μm, they were still very thick with the thickness spanning from 50 to 300 nm (Fig. 4d).

The advantages and disadvantages for the synthesis of 2D perovskites are shown in Table 1. Nevertheless, even if the synthesis of 2D perovskites have drawn the substantial attention and made the significant progress, the obtained 2D perovskites were mostly configured in the sheet-like morphology without good control of their thickness, which seriously restricted their applications in electronics and optoelectronics. New synthesis methods towards the controlled synthesis with well-defined thickness and large lateral size are urgently preferred in the near future to industrialize these 2D materials.
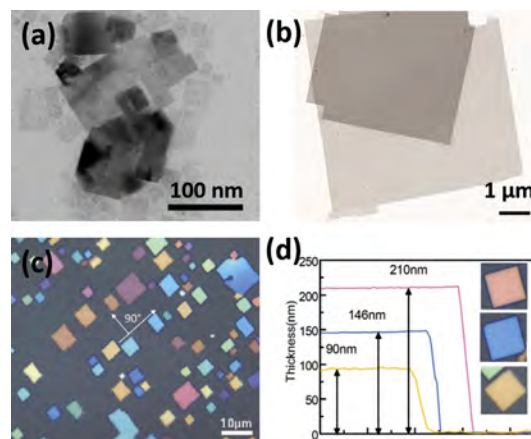

Fig. 4. Inorganic halide perovskites flakes. (a) TEM image of $CsPbBr_3$ nanoplates synthesized by colloidal method. Reproduced with permission from Ref. [60]. Copyright 2015, American Chemical Society. (b) TEM image of large lateral size $CsPbBr_3$ nanoplates. Reproduced with permission from Ref. [63]. Copyright 2016, American Chemical Society. (c) Optical microscopy image of $CsPbBr_3$ flakes on Mica. (d) AFM line profile of the $CsPbBr_3$ flakes with different color. (c), (d) Reproduced with permission from Ref. [64]. Copyright 2016, WILEY-VCH.

Table 1
Advantages and disadvantages of the synthesis methods.

Materials	Synthesis methods	Advantages	Disadvantages
Organic—inorganic mixed halide perovskites	Chemical conversion	Large lateral size; high crystal quality	Poor control in thickness
	Direct CVD	Large lateral size; high crystal quality	Poor control in thickness
2D RP perovskites	Mechanical exfoliation	High crystal quality	Small lateral size; lack of control in thickness; low production
	Liquid exfoliation	Large amount of production	Small lateral size; lack of control in thickness; poor crystal quality
	Solution based method	Large amount of production; high crystal quality	Small lateral size; poor crystal quality; poor control in thickness; substrate needed
	Colloidal based method	Large amount of production; fine control of flake thickness	Small lateral size; poor crystal quality
	CVD	High crystal quality; large lateral size	Lack of control in thickness
Inorganic halide perovskites	Colloidal based method	Large production	Poor control in thickness
	CVD	High crystal quality; large lateral size	Lack of control in thickness

4. Optoelectronic properties of 2D halide perovskites

For practical device applications, the most interesting optoelectronic properties of 2D materials are the large exciton binding energy due to the reduced dielectric screening (i.e. image charge effect) and quantum confinement effect. For example, monolayer WS_2 has exciton binding energy as large as 700 meV [66]. In 2D perovskites, large exciton binding energies are also observed in 2D RP perovskites. Early reports have found that the excitons were mostly existed as the Wannier-type and the exciton binding energy of single layer ($n = 1$) 2D RP perovskites is usually in a range of about 170—480 meV depending on the encapsulating organic layer [67—72]. This large exciton binding energy is typically higher than the thermal energy at room temperature ($k_BT = 25.7$ meV), which means that the photogenerated electron—hole pairs are bound together by Coulombic attraction forming excitons, being stable at room temperature and difficult to be ionized by thermal fluctuation. This way, the excitonic absorption of 2D RP perovskites can be obviously observed at room temperature as a strong and sharp peak below the band gap onset (Fig. 5a).

Due to the different dielectric environment, the exciton binding energy of atomically thin 2D RP perovskites is somewhat different from their bulk counterparts. Yaffe et al. have found that the binding energy of atomically thin BA_2PbI_4 (a single unit cell thick 2D material) is as high as 490 meV [50]. This value is already much higher than its bulk material configured with single layers of corresponding 2D RP perovskite (360 meV), which was attributed to the different dielectric environment. The exciton binding energy is also highly depended on the layer numbers (i.e. the quantum well width), in which the 2D RP perovskites with larger n would have the smaller exciton binding energy because of the reduced quantum confinement effect [73—75].

Moreover, the exciton binding energy can as well be roughly determined from the difference between the first exciton absorption peak and the onset of absorption from corresponding absorption spectrum at low temperature as shown in Fig. 5b [76—78].
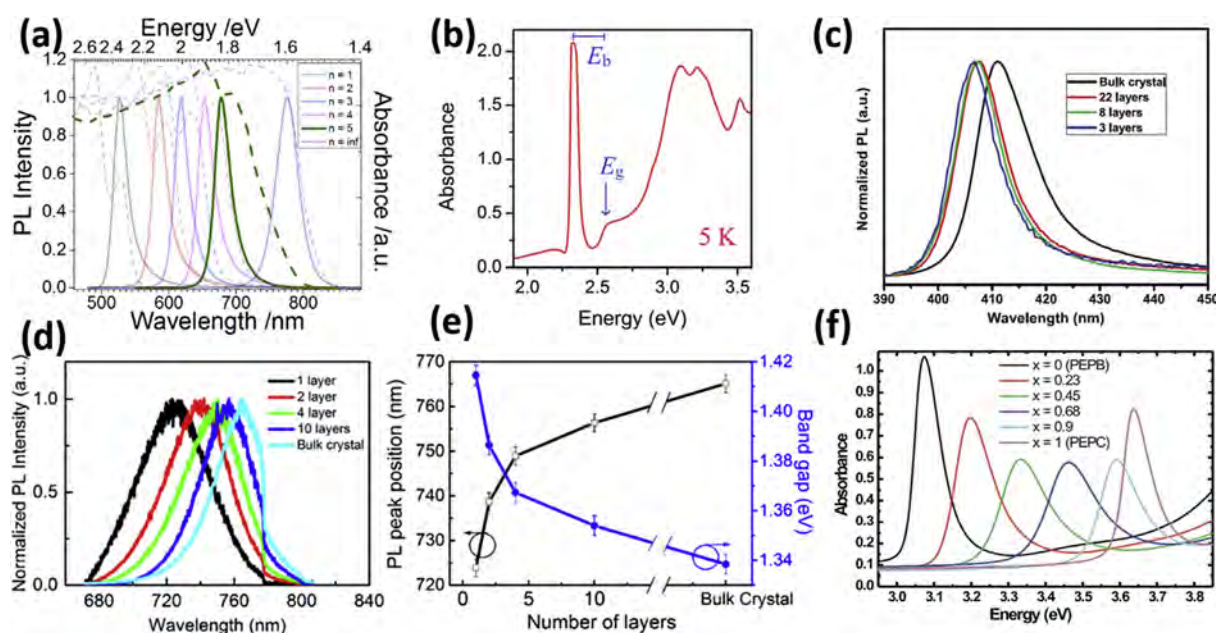

Fig. 5. Optoelectronic properties of 2D halide perovskites. (a) PL and absorption spectra of $BA_2MA_{n-1}Pb_nI_{3n+1}$ with different n values at room temperature. Reproduced with permission from Ref. [74]. Copyright 2017, Elsevier Inc. (b) Absorption spectrum of a representative 2D perovskite at 5 K. Reproduced with permission from Ref. [76]. Copyright 2018, Royal Society of Chemistry. (c) PL spectra of BA_2PbBr_4 with different thicknesses. Reproduced with permission from Ref. [50]. Copyright 2015, American Association for the Advancement of Science. (d) PL spectra of $MAPbI_3$ nanosheets with different thicknesses. (e) PL peak position and band gap as a function of the number of unit cells in the perovskite. (d), (e) Reproduced with permission from Ref. [44]. Copyright 2016, American Chemical Society. (f) Absorption spectra of $PEA_2PbBr_{4(1-x)}Cl_{4x}$. Reproduced with permission from Ref. [81]. Copyright 2014, American Chemical Society.

However, it is rather difficult to obtain the accurate exciton binding energy from the room temperature absorption spectrum owing to the thermal broadening of the spectrum. It is important to point out that Tauc plot cannot be used to determine the band gap of 2D RP perovskites for two reasons. First, the absorption spectrum contains the exciton absorption peak, which always merges with the onset of the absorption spectrum from band gap transitions at room temperature. Second, the relation $\alpha h\nu \propto (h\nu - E_g)^{1/2}$ is not valid for 2D materials due to the difference of the joint density states of 3D and 2D materials [79]. Fortunately, since the absorption of 2D materials is step-like near the band gap [79], in this case, the band gap of 2D RP perovskites can be determined from the step-like onset of the absorption spectrum at low temperature as demonstrated in Fig. 5b [77].

Importantly, the large exciton binding energy of 2D RP perovskites make them suitable for light emitting devices owing to the increased radiative recombination probability and the sharp exciton emission peak. In fact, 2D RP perovskites also have the high photoluminescence (PL) quantum yield. Yuan et al. have found that the PL quantum yield of colloidal 2D RP perovskite microdisks was up to 53% with a narrow deep blue emission [80]. Because of the large exciton binding energy, the 2D RP perovskites typically have a fast radiative recombination of photo-generated carriers. This way, the charge carrier lifetime is short as compared with the ones of 3D perovskites, ranging in several to tens of nanoseconds [81]. For large n values (>2), the 2D RP perovskites showed another interesting photo-physics phenomenon, which is the dissociation of excitons into free carriers at lower energy edge states [49]. In other words, once the carriers were trapped in the edge states, they remained protected and did not lose their energy through non-radiative processes, contributing to the photocurrent in photovoltaic devices or radiatively recombining efficiently as desired for light emission devices. Thus, this behavior can substantially improve the performance of fabricated optoelectronic devices.

Interestingly, the band gap of 2D RP perovskites reduces with the increasing of layer numbers (n values) due to the reduced quantum confinement effect [74]. The combined effects of band gap and exciton binding energy on layer numbers affect both the absorption and photoluminescence spectra of 2D RP perovskites, making it more difficult to extract optical parameters. Anyway, the excitonic absorption peak and the photoluminescence peak shift to the low energy side were observed with the increasing layer number of n (Fig. 5a) [75]. Recently, Blancon et al. carried out a systematical study on the dependence of exciton properties on the value of n of the 2D perovskite $BA_2MA_{n-1}Pb_nI_{3n+1}$ using optical spectroscopy and 60-T magnetoabsorption supported by modeling and found both the band gap and the exciton binding energy decreased with the increasing of n accompanied by the decreasing of the exciton reduced mass [82]. In addition, the band gap of 2D RP perovskites also depends weakly on their physical thicknesses. As illustrated in Fig. 5c, the emission peak of BA_2PbBr_4 sheets shifted to the lower wavelength as their physical thicknesses increase [51]. The blue shift of the PL peak was probably attributed to the structural relaxation of the in-plane crystal lattice, indicating that the van der Waals interaction between layers could also affect the electronic properties of the RP 2D perovskites even though the interaction was very weak. Similar results were also observed in PEA_2PbI_4 [54].

Similar with other 2D semiconducting inorganic semiconductors, the band gap of atomically thin $MAPbI_3$ was found to decrease with the increase of layer numbers [45]. The PL emission peak for one single layer of $MAPbI_3$ was centered at ~720 nm, and it gradually increased to the bulk value of ~765 nm (Fig. 5d). The PL peak and band gap were observed to change with the thickness of $MAPbI_3$ nanoplates as shown in Fig. 5e. The enlarged band gap of

ultra-thin $MAPbI_3$ nanoplates could be attributed to the quantum confinement effect. However, the band gap of monolayer $MAPbI_3$ was still much smaller than that of single layer 2D RP perovskites. The only difference between monolayer $MAPbI_3$ and single-layer 2D RP perovskites is the existence of organic encapsulating layer in 2D RP perovskites, which may lead to the lattice distortion of the inorganic layer. Therefore, the reasons for having the different band gap here may be ascribed to the different dielectric environment and lattice distortion.

Like 3D perovskites, the absorption spectrum of 2D RP perovskites could also be well tuned by the partial substitution of halide cations, which made them suitable for tunable wavelength LEDs and tandem solar cells. Lanty et al. have reported that the excitonic absorption of PEA_2PbX_4 (X = I, Br) could be well manipulated by the partial substitution of Br with Cl as shown in Fig. 5f [83]. The tunable absorption was ascribed to the band gap tuning by the partial substitution of cations. Weidman et al. have as well found that the emission energy and absorption spectra of RP perovskite nanoplatelets with the chemical formula $L_2A_{n-1}B_nX_{3n+1}$ could be varied by changing the n values, B halide cation and X anion, while the variation of A cation would lead to only subtle changes [84]. Furthermore, mixed halide nanoplatelets exhibited the continuous spectral tunability all the way from 2.2 to 3.7 eV, covering a spectral range of 1.5 eV.

5. Energy applications

Among many exciting characteristics of 2D perovskites, the excellent optoelectronic properties, such as the large absorption coefficient, high carrier mobility and long diffusion length, make them promising for energy-related applications. Till now, great achievements have been made in various energy-related utilizations. Here, we summarize the recent progresses of 2D perovskites for energy-related devices, including photodetectors, LEDs, and solar cells.

5.1. Photodetectors

In general, 2D $MAPbI_3$ flakes is suitable as the active material for photodetectors because of its large absorption coefficient, high carrier mobility, and small exciton binding energy (<26 meV). For instance, Wang et al. fabricated photodetector arrays based on $MAPbI_3$ microplates [46]. The obtained photodetectors showed a low dark current (on the order of pA) and nearly linear current—voltage behavior under illumination with the wavelength of 488 nm (Fig. 6a), indicating the excellent photoresponse of the perovskite crystals. The photocurrent-to-dark current ratio of devices could reach up to three orders of magnitude. Notably, the responsivity of fabricated photodetectors was found to be ~7 A W^{-1} under a bias voltage of 5 V, corresponding to a photogain of ~18. The devices also had a fast photoresponse with both rising and falling times in the range of ~500 μs (Fig. 6b). By further reducing the channel length from 8 μm to 100 nm, the responsivity could be improved to ~40 A W^{-1}. At the same time, Liu reported that atomically thin 2D $MAPbI_3$ photodetectors as well showed the wide band response, spanning from ultraviolet to the entire visible spectral range [45]. The device showed linear $I-V$ curves with and without light illumination (Fig. 6c), indicating the good contact between the gold electrodes and the perovskite. The photocurrent-to-dark current ratio can reach up to 2 orders of magnitude as shown in the inset of Fig. 6c. The responsivity of the photodetectors was high with a bias voltage of 1 V, which was 22 A W^{-1} at 405 nm (Fig. 6d), and 12 A W^{-1} at 532 nm. The rise and decay times of the photodetectors were shorter than 20 and 40 ms, respectively (Fig. 6e). Interestingly, Lan et al. found that photodetectors made
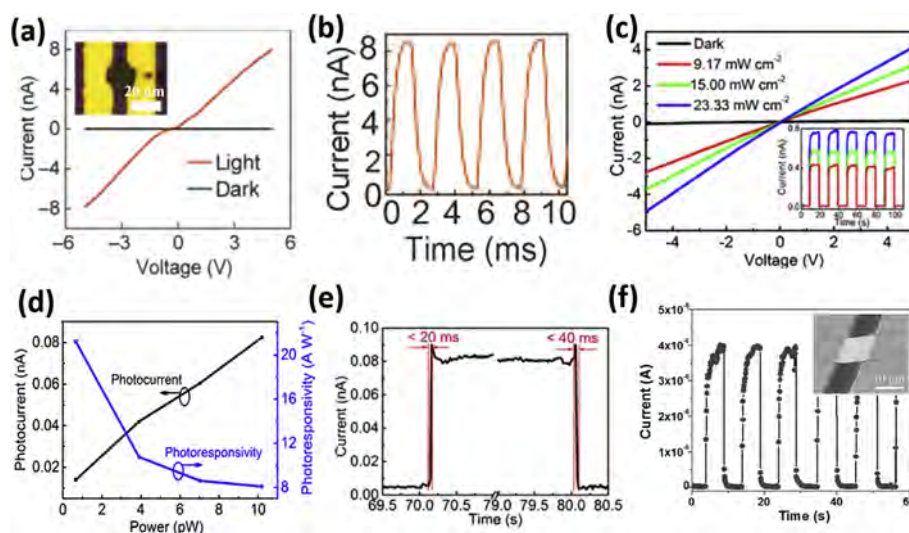
Fig. 6. Photodetectors based on MAPbI$_3$ flakes. (a) $I-V$ curve of the MAPbI$_3$ nanosheet based photodetector with and without light illumination (488 nm). Inset: corresponding optical microscopy image of the device. Scale bar: 20 μm. (b) Response speed of a typical two-probe device with 488 nm modulated light illumination. (a), (b) Reproduced with permission from Ref. [45]. Copyright 2015, American Association for the Advancement of Science. (c) $I-V$ curve of the MAPbI$_3$ sheet based photodetector with and without light illumination (405 nm). Inset: Time-dependent current under modulated light illumination (405 nm) with a bias voltage of 1 V. (d) Photocurrent and photoresponsivity as a function of incident power at a wavelength of 405 nm. (e) Temporal photocurrent response excited at 405 nm. (c), (d), (e) Reproduced with permission from Ref. [44]. Copyright 2016, American Chemical Society. (f) Current as a function of time under modulated light illumination (405 nm) under the bias voltage of 5 V. Inset: corresponding SEM image of the device. Reproduced with permission from Ref. [22]. Copyright 2017, WILEY-VCH.

from free-standing MAPbI$_3$ nanosheets had the decent photo-response [22]. The fabricated photodetector had the good stability under chopped light illumination with the high on/off ratio of 400 (Fig. 6f). The responsivity of the photodetector (with the channel length of 8 μm as shown in the inset of Fig. 6f) was about 40 A W^{-1} under 405 nm light illumination and bias voltage of 5 V, which was close to the responsivity of microplate MAPbI$_3$ with the ultra-small channel length (100 nm) [46], indicating the excellent performance of the obtained photodetector. On the other hand, Li et al. fabricated MAPbI$_3$ nanosheet based photodetectors based on the vertical configuration using Au and indium tin oxide as electrodes [85]. Although the photodetectors showed the relatively low responsivity (36 mA W^{-1} at 635 nm), it provided another device scheme for the photodetector design with different configurations.

Simultaneously, 2D RP perovskites also showed the excellent photodetection performance. Zhou et al. have made photodetectors from RP perovskite BA$_2$MA$_{n-1}$Pb$_n$I$_{3n+1}$ films [86]. The RP perovskite film showed the n dependent response spectrum, being consistent with the absorption spectrum. Once configured into photodetectors, the photocurrent was highly depended on the inner perovskite layer thickness, where the better photodetection performance was observed in the film with the large n value (Fig. 7a). In specific, the responsivity with $n = 1, 2,$ and 3 was measured to be 3.00, 7.31, and 12.78 mA W^{-1}, respectively, under white light illumination with a power of 3.0 mW cm^{-2}. All the photodetectors had a fast photoresponse with the response time in milliseconds. The polycrystalline nature of 2D RP perovskites might be the reason for the observed low responsivity. Recently, we have found that the photodetection performance of 2D RP perovskites could be significantly improved by the substitution of the long direct chain BA$^+$ with branched i-BA$^+$ and using a hot-casting processing method [87]. Particularly, the photodetectors based on hot-casting (i-BA)$_2$MA$_3$Pb$_4$I$_{13}$ films had a high responsivity of 117 mA W^{-1} under a bias voltage of 1.5 V (Fig. 7b). Furthermore, the response speed was very fast, with the rise time of 16 ms and decay time of 15 ms (Fig. 7c). These high responsivity and fast response were attributed to the improved crystal quality of films prepared by hot-casting

method. The branched encapsulating cations with short chain lengths was thought to be another performance enhancement reason because the short chain cations could facilitate the efficient carrier transport between layers. The reduced exciton binding energy with the large n values might also contribute to the enhanced performance. For photodetectors, single crystalline active sensing materials (i.e. with good crystallinity) are highly preferred due to the reduced defects and hence the longer carrier lifetime. Tan et al. reported the first photodetector based on ultra-thin 2D (BA)$_2$PbBr$_4$ perovskite single crystals with graphene as electrodes (inset of Fig. 7d) [88]. The photodetector showed the remarkable photocurrent for wavelengths smaller than 510 nm (Fig. 7d), which corresponded to the band gap of the 2D perovskite. For further optimizing the photoresponse, interdigital graphene electrodes were designed and implemented (Fig. 7e) to enhance the absorption cross section of 2D perovskite crystals. The distance between each pair of graphene electrodes was about 100 nm while the entire 2D perovskite crystal acted as a light sensitive material underneath graphene. The device showed the good stability upon photoswitching with an on/off current ratio of 10^3 (Fig. 7f), indicating the excellent photodetection performance of the device. In fact, the device showed an ultrahigh responsivity of up to 2100 A W^{-1} under a small bias voltage of 0.5 V. The ultra-short channel length (100 nm) might account for the ultra-high responsivity because the device was operated in the ballistic regime. In any case, this ultra-short channel length was hard to be realized for most of the practical applications. It is also hard to obtain 2D RP perovskite single crystals with the large lateral dimension. The interfacial charge-carrier scattering existed in stacked nanosheets and the undesired quantum confinement effect could seriously reduce the performance of corresponding photodetectors. In view of these issues, Yu et al. proposed a novel post-synthetic treatment method to tackle the problems in order to obtain the excellent photodetection performance [89]. In explicit, 2D OA$_2$FA$_{n-1}$Pb$_n$Br$_{3n+1}$ microplatelet film could be immersed in solution containing FA$^+$, leading to the improvement in two aspects as schematically shown in Fig. 7g. First, the dimensionality of 2D perovskites was increased
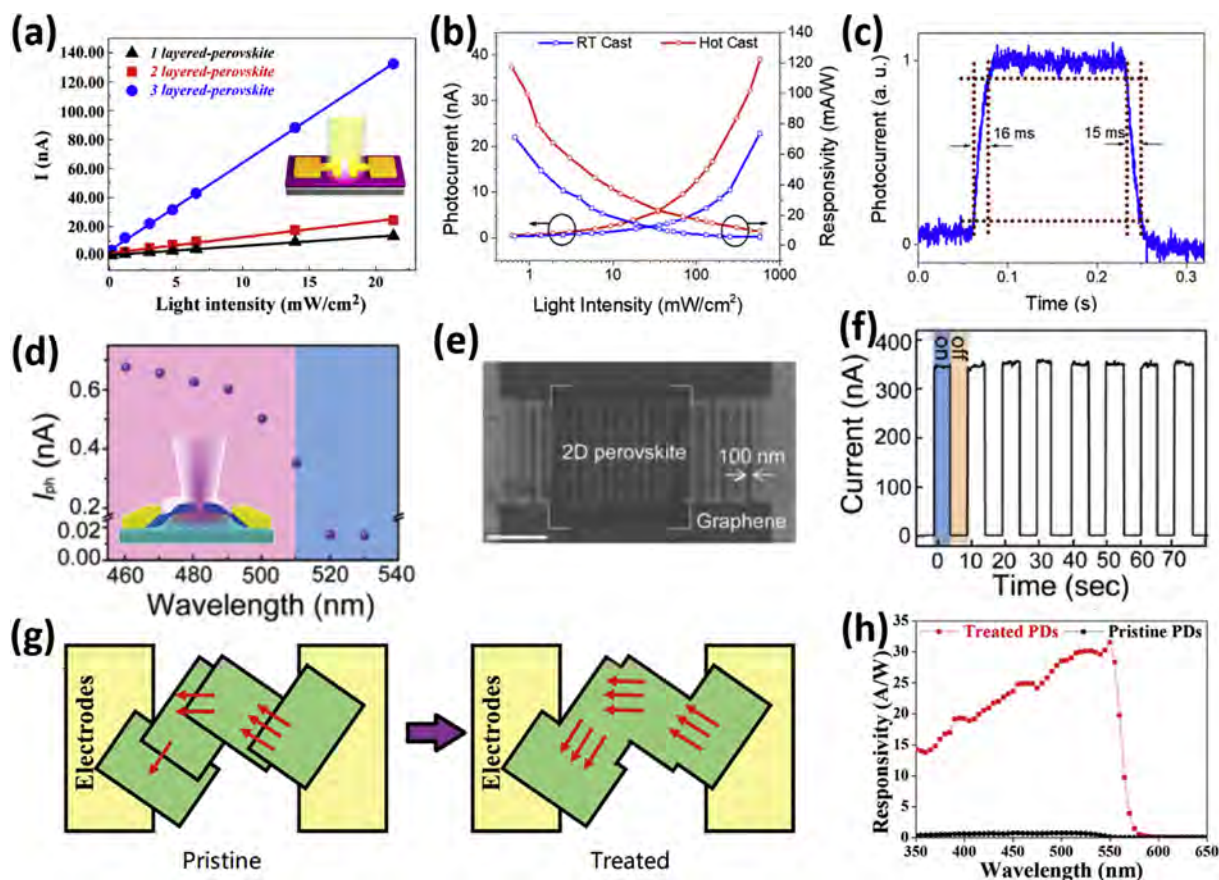
Fig. 7. Photodetectors based on 2D RP perovskites. (a) Photocurrent as a function of light intensity for different layered perovskites with a bias voltage of 30 V. Inset: corresponding illustrative schematic of the fabricated photodetector. Reproduced with permission from Ref. [84]. Copyright 2016, American Chemical Society. (b) Photocurrent and responsivity versus light intensity (532 nm) under a bias voltage of 1.5 V. (c) High-resolution photocurrent versus time. (b), (c) Reproduced with permission from Ref. [85]. Copyright 2018, American Chemical Society. (d) Photocurrent versus wavelength under a fixed incident power. Inset: Corresponding illustrative schematic of the measured photodetector. (e) SEM image of the photodetector. Scale bar: 1 μm. (f) Time dependent photocurrent response of the photodetector measured with a 470 nm defocused laser. (d)–(f) Reproduced with permission for Ref [86]. Copyright 2016, American Chemical Society. (g) Illustrative schematic of the pristine and treated 2D $OA_2FA_{n-1}Pb_nBr_{3n+1}$ microplatelet film photodetector. (h) Responsivity as a function of wavelength for both treated and pristine 2D $OA_2FA_{n-1}Pb_nBr_{3n+1}$ microplatelet film photodetectors. (g), (h) Reproduced with permission from Ref. [87]. Copyright 2017, American Chemical Society.

through an exchange reaction between OA^+ and FA^+, which meliorated the quantum confinement effect and facilitated the separation of electrons and holes. Second, the free-standing 2D perovskites platelets were fused for promoted interdomain charge-carrier transport. The treated photodetectors could then achieve a responsivity up to 32 A W^{-1} (Fig. 7h) and the rise/decay time was shortened by two orders of magnitude down to 0.25 and 1.45 ms, respectively.

Moreover, inorganic 2D perovskites also showed the impressive photosensing properties. Song et al. utilized $CsPbBr_3$ ultra-thin sheets (1–3 layers) to fabricate flexible photodetectors on poly-ethylene terephthalate (PET) substrates (Fig. 8a) [63]. In detail, a centrifugal casting method with $CsPbBr_3$ nanosheet dispersion was used to assemble $CsPbBr_3$ nanosheet based films on the patterned indium tin oxide (ITO)/PET substrates, where ITO was employed as the electrode. The responsivity versus wavelength curves under different bias voltages are then shown in Fig. 8b, where the maximum responsivity appeared at 517 nm, and the responsivity was about 0.65 A W^{-1} when the bias voltage was 10 V. Also, the photodetectors exhibit the ultra-fast photoresponse with the rise and decay times of 19 and 25 μs, respectively (Fig. 8c). Notably, the photodetectors as well demonstrated the excellent stability and the outstanding flexibility with negligible degradation even after 10,000 bending cycles (Fig. 8d). The low responsivity of the

photodetectors could be attributed to the small lateral size of the obtained nanosheets (several hundred nanometers) and the wide channel length (20 μm), where the interboundary hopping process of carriers among adjacent sheets is inevitable. This way, the same group employed a modified method to synthesize $CsPbBr_3$ nano-platelets with lateral size as large as 10 μm, which was then utilized to fabricate photodetectors [90]. Because the nanoplatelets were large enough, they could effectively bridge across the channel between two metal electrodes for the carrier transport (Fig. 8e). As a result, the performance of fabricated photodetectors were much improved with a high responsivity of 34 A W^{-1} (Fig. 8f) and a specific detectivity of 7.5×10^{12} Jones under a bias voltage of 1.5 V at 442 nm. This superior photodetector performance was mostly due to the strong light absorption and the excellent in-plane charge carrier transport of spatially-scattered multilayer $CsPbBr_3$ nano-platelets. At the same time, this group also used another approach to tackle the low carrier transport resulting from the small lateral size of nanoplatelets, in which they hybridized $CsPbBr_3$ nano-platelets with carbon nanotubes (CNTs) (Fig. 8g) [91]. These hybrid films could be simply obtained by a drop-casting method utilizing the CNTs-$CsPbBr_3$ dispersion. The fast evaporation of the solvent prevented the precipitation of CNTs, forming a uniform composite film. As a result, the highest responsivity of optimized composite films was measured to be 31.1 A W^{-1} under a bias of 10 V (Fig. 8h).
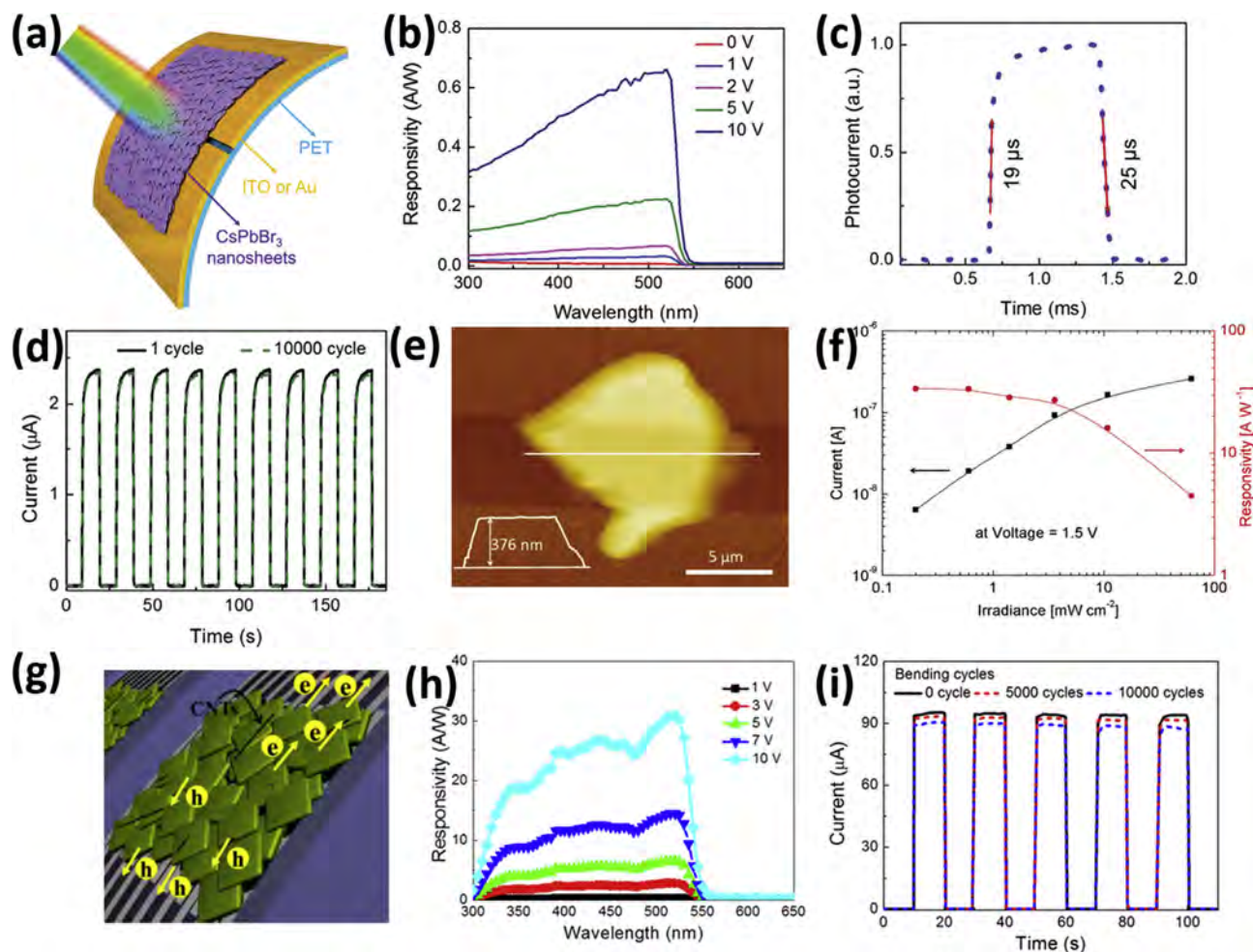
Fig. 8. Photodetectors based on inorganic perovskites. (a) Illustrative schematic of the CsPbBr$_3$ sheet based flexible photodetecotors. (b) Responsivity as a function of wavelength under different bias voltages. (c) High-resolution photocurrent versus time curve under modulated light illumination. (d) Current versus time under modulated light illumination. (a)–(d) Reproduced with permission from Ref. [62]. Copyright 2016, WILEY-VCH. (e) AFM image of the photodetector with a single multilayer CsPbBr$_3$ nanoplatelet bridging across two metal electrodes. (f) Photocurrent and photoresponsivity versus irradiance. (e), (f) Reproduced with permission from Ref. [88]. Copyright 2017, WILEY-VCH. (g) Illustrative schematic of the CNT/CsPbBr$_3$ hybrid film flexible photodetector. (h) Responsivity as a function of wavelength under different bias voltages. (i) Current versus time under modulated light illumination after different bending cycles. Reproduced with permission from Ref. [89]. Copyright 2017, American Chemical Society.

The fabricated photodetectors as well had a fast response with a rise time of 16 μs owing to the efficient charge extraction and transport assisted by CNTs. Furthermore, the photodetectors exhibit the excellent flexibility, where the photocurrent only showed a decrease of ~6.4% after 10000 bending cycles (Fig. 8i).

For better comparison and understanding of the 2D perovskite photodetectors, the performance parameters of some typical photodetectors are listed in Table 2. The high performance of the photodetectors indicates that 2D perovskites are suitable for photodetection applications.

5.2. LEDs

Since 2D perovskites have the large exciton binding energy (>26 meV) and high PL quantum yield, they are also suitable for LED applications. The earliest report about LEDs based on RP 2D perovskites can be traced back to the mid-1990s [92,93]. For example, Era et al. have fabricated the first RP 2D perovskite (PEA$_2$PbI$_4$) based LEDs, which showed a sharp emission at 520 nm with a full width at half maximum (FWHM) of 10 nm at liquid-nitrogen temperature with high luminescence (10,000 cd m^{-2} at 24 V) [92]. However, the room temperature electroluminescence efficiency was very small,

which could be the result of the thermal ionization of excitons there. In any case, the low operating temperature significantly restricted its further development.

Recently, with the growing interest of perovskites in LEDs, 2D RP perovskites have regained the attention. Many researchers found that the LED devices based on single component 2D RP materials could work efficiently at room temperature, but the external quantum efficiency (EQE) was still low [94,95]. For example, Liang et al. reported the deep blue (410 nm) LEDs based on (PEA)$_2$PbBr$_4$ nanoplates with the device structure of ITO/ PEDOT:PSS (30 nm)/PEA$_2$PbBr$_4$/TPBi (35 nm)/Ca (25 nm)/Al (100 nm) (Fig. 9a) [94]. These devices exhibited the strong light emission with an ultra-narrow FWHM of 14 nm (Fig. 9b) with an EQE of 0.04%, which was impressively high for the deep blue LEDs. The enhanced EQE was attributed to the conversion of polycrystalline PEA$_2$PbBr$_4$ films into single-crystal nanoplates via DMF solvent vapor annealing (Fig. 9c). Li et al. also reported (C$_6$H$_5$CH$_2$NH$_3$)$_2$PbI$_4$ based multilayer LED devices, which emitted light at 526 nm with a narrow FWHM of 15 nm [95]. These devices gave a luminescence of ~9 cd m^{-2} at 5 V with a low EQE of 0.005%. Furthermore, these devices were not stable and could only work for 1 min. The reason for this low EQE was not well understood so far,

Table 2
Typical 2D perovskites based photodetectors.

Material	Bias voltage (V)	Light wavelength (nm)	Responsivity (A W^{-1})	Speed (s)	Ref.
MAPbI$_3$ microplate	5	488	7 (8 μm channel length)	500 μ	[46]
			40 (100 nm channel length)	—	
Single layer MAPbI$_3$ sheet	1	405	22	40 m	[45]
		532	12	—	
MAPbI$_3$ nanosheets	5	405	40	1.4	[22]
BA$_2$MA$_{n-1}$Pb$_n$I$_{3n+1}$ film	30	White light	3.00 m ($n = 1$)	27.5 m	[86]
			7.31 m ($n = 2$)	8.4 m	
			12.78 m ($n = 3$)	10.0 m	
i-BA$_2$MA$_3$Pb$_4$I$_{13}$ film	1.5	532	117 m	16 m	[87]
BA$_2$PbBr$_4$ sheet	0.5	510	2100	—	[88]
Fused OA$_2$FA$_{n-1}$Pb$_n$Br$_{3n+1}$ microplatelet film	9	550	32	1.45 m (442 nm)	[89]
CsPbBr$_3$ nanosheets film	10	517	0.65	25 μ (442 nm, 5 V)	[63]
CsPbBr$_3$ nanoplatelet	1.5	442	34	0.9 m	[90]
CsPbBr$_3$ nanoplatelet-CNT hybrid film	10	517	31.1	0.38 m (442 nm, 3 V)	[91]

which might be partly due to the strong exciton–phonon coupling in single-layer 2D RP perovskites [96].

For 2D RP perovskites, it is usually difficult to obtain pure phase materials for $n \geq 2$. However, several groups found that LEDs made from mixed phase 2D RP perovskites could yield the excellent performance as compared with the one made with single component counterparts [97–103]. It was also found that in mixed phase 2D RP perovskites with different n values, the photo-generated carriers would have a tendency to transfer to the large n value perovskite with the small band gap as shown in Fig. 9d due
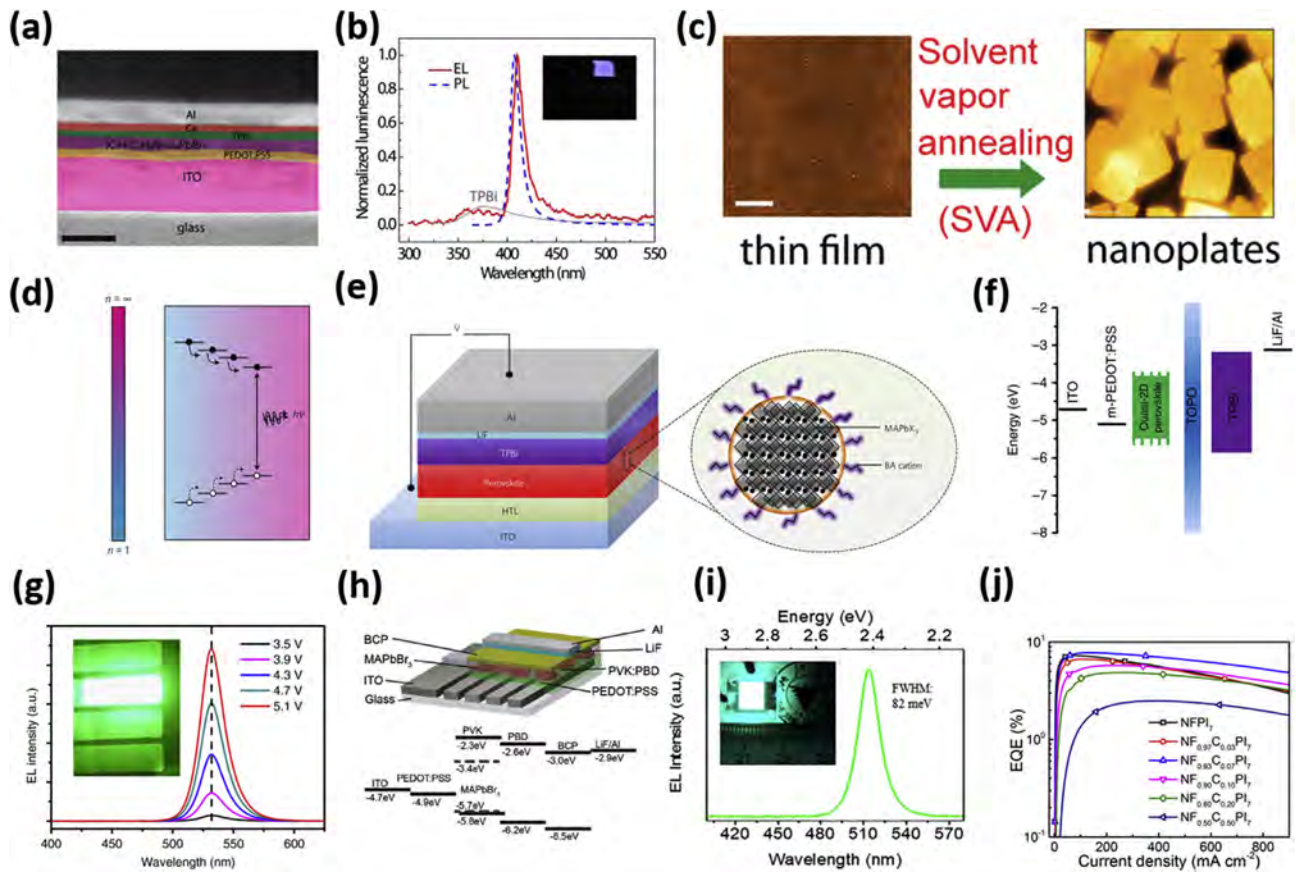

Fig. 9. LED device structures and performances. (a) Cross-sectional SEM image of the PEA$_2$PbBr$_4$ LED devices. (b) Normalized luminescence of a typical LED device based on PEA$_2$PbBr$_4$ nanoplatelets obtained from DMF vapor with annealing operated at 6 V. (c) AFM image of the pristine and annealed PEA$_2$PbBr$_4$ films. (a)–(c) Reproduced with permission from Ref. [92]. Copyright 2016, American Chemical Society. (d) Multi-phase perovskite materials (PEA$_2$MA$_{n-1}$Pb$_n$I$_{3n+1}$) channel energy across an inhomogeneous energy landscape, concentrating carriers to the smallest band gap emitters. The arrow represents the carrier transfer process. Reproduced with permission from Ref. [95]. Copyright 2016, Macmillan Publishers Limited, part of Springer Nature. (e) Device structure of the perovskite LEDs. A schematic of a nanometer-sized grain with BA cations decorating its surface is shown on the right. Reproduced with permission from Ref. [98]. Copyright 2016, Macmillan Publishers Limited, part of Springer Nature. (f) Band alignment of each function layer in the LED devices. (g) Typical electroluminescence spectra of PEA$_2$Pb$_{n-1}$Pb$_n$Br$_{3n+1}$ ($n = 3$ composition) based LEDs under different voltage biases. Inset shows the electroluminescence image of LEDs. (f), (g) Reproduced with permission from Ref. [99]. Copyright 2018, Macmillan Publishers Limited, part of Springer Nature. (h) Device architecture for a LED with perovskite nanoplatelets as the emitter, and the flat-band energy level diagram of different layers of materials, showing conduction and valance band levels with respect to vacuum. Reproduced with permission from Ref. [102]. Copyright 2016, WILEY-VCH. (i) Electroluminescence spectrum at an applied bias of 4 V. Inset shows a photograph of a 56 mm^2 device. Reproduced with permission from Ref. [104]. Copyright 2017, American Chemical Society. (j) EQE versus current density. Reproduced with permission from Ref. [107]. Copyright 2018, American Chemical Society.

to their special band alignment [97–99]. This way, high EQE were observed in the mixed phase 2D RP perovskites based LED devices. For example, Yuan et al. have discovered that the mixed 2D RP perovskites ($PEA_2MA_{n-1}Pb_nI_{3n+1}$) with the optimized composition based LEDs exhibited a high EQE of 8.8% and a radiance of 80 W sr^{-1} m^{-2} [97]. They anticipated that the layered perovskite materials functioned as charge carrier concentrators, ensuring that the radiative recombination successfully outcompetes the trapping and hence the non-radiative recombination. Wang et al. also reported LEDs based on mixed 2D RP perovskites of $NMA_2FA_{n-1}Pb_nI_{3n+1}$ (NMA = $C_{10}H_7CH_2NH_3^+$) with partial substitution of I with Br with a high EQE of 11.7%, good stability and exceptional high power performance [99]. Specifically, the lower band gap regions that generated electroluminescence were effectively confined by perovskite multiple quantum wells with the higher energy gaps, which was thought to be the reason for the outstanding performance. Furthermore, Xiao et al. used thick $BA_2MA_{n-1}Pb_nX_{3n+1}$ (X = Br, I) nano-crystal (n ~ 19) based films as the emitting layers in LEDs (Fig. 9e), which were very smooth in the surface morphology and showed the excellent performance with a high EQE of 10.4% for X = I (emission at 748 nm) and 9.3% for X = Br (emission at 513 nm) [100]. These ultra-small crystal grains were believed to lead to the high EQE. More importantly, these LEDs had the exceptional stability, where their performance could be maintained after storage for more than 8 months. The ultra-smooth, pinhole-free and compact perovskite films as well as the bulky nature of the long alkyl chains could effectively stabilize the crystallite surfaces there for the much enhanced stability. By optimizing the composition of $PEA_2FA_{n-1}Pb_nBr_{3n+1}$ and adding a layer of trioctylphosphine oxide (TOPO) on the surface of the perovskite film as passivation (Fig. 9f), Yang et al. realized a high EQE of 14.36% and a high luminescence of 9120 cd m^{-2} at 532 nm (Fig. 9g) [101]. These LEDs could continuously work for 120 min, indicating the good stability of the devices. Quan et al. have tailored the mixed-n 2D perovskites to govern the energy transfer into the lowest-band gap minority phase while to do so faster than it is lost to nonradiative centers [104]. This way, the photoexcited states were concentrated into a small subpopulation of radiative domains, leading to a high quantum yield, even at low excitation intensities. LED based on these mixed 2D perovskites exhibited an EQE of 7.4% and a high luminescence of 8400 cd m^{-2}.

Recently, many researchers developed other approaches to further enhance the stability and efficiency of 2D RP perovskite based LEDs, such as dispersing the 2D RP perovskites in organic matrix. For instance, Ling et al. fabricated $OA_2MA_{n-1}Pb_nBr_{3n+1}$ nanoplatelet based room-temperature efficient green LEDs that exhibited a high luminescence of 10,590 cd m^{-2} at 12 V [105]. The device structure is also illustrated in Fig. 9h, In specific, $OA_2MA_{n-1}Pb_nBr_{3n+1}$ nanoplatelets were dispersed in poly(9-vinylcarbazole):2-(4-biphenylyl)-5-phenyl-1,3,4-oxadiazole (PVK:PBD) bipolar organic host, which acted as the emitting layer. The remarkable brightness of obtained LEDs were attributed to the optimized charge balance in the emitting layer using composition-tailored bipolar host PVK:PBD. However, the corresponding EQE was still low (0.48%). At the same time, Kumar et al. employed the same nanoplatelets and device structure to fabricate LEDs [106]. They could control the n value, which is the thickness of the nanoplatelets; therefore, the emitting wavelength could be reliably tuned. This way, pure green emission at 520 nm for n = 8–11, sky blue emission at 492 nm for n = 6, pure blue emission at 456 for n = 4, and deep blue emission at 432 nm for n = 2 LEDs were successfully realized. Furthermore, the LED devices showed the high EQE (pure green emission, 2.31%) due to the well-separated 2D perovskites in the organic matrix as well as the flatter emission layer.

Other 2D RP perovskites, where the interior perovskite layer is totally inorganic, were also used in the fabrication of high efficiency LEDs due to their naturally established quantum well structure. Si et al. reported the first single layer $PEA_2Cs_{n-1}Pb_nX_{3n+1}$ (X = Br, I, n is was in the range of 12–16) based LEDs [107]. The fabricated LEDs showed the high color purity (Fig. 9i) with the remarkably high EQE (514 nm, 10.4% for X = Br, and 683 nm, 7.3% for X = I). Huang's group have then studied the mixed phase $NMA_2Cs_{n-1}Pb_nI_{3n+1}$ based LEDs in detail [108–110]. They found that the incorporation of Cl in $NMA_2Cs_{n-1}Pb_nI_{3n+1}$ would favor the growth of larger-n quantum wells and improved the crystallinity, which led to the enhanced EQE (3.7%) and moderate luminance (440 cd m^{-2}) at 688 nm [108]. The overall performance of the mixed phase $NMA_2Cs_{n-1}Pb_nI_{3n+1}$ based LEDs could be significantly enhanced by tailoring the dimensionality of perovskite quantum wells through changing the ratio of large cations to small cations in precursor solutions. The LEDs emitted red light at 694 nm with a luminance of 732 cd m^{-2} and a maximum EQE of 7.3%. The energy transfer from the small n with the larger band gap to the large n with the smaller band gap was also thought to be a key contribution to the obtained high EQE [109]. Lately, they also found that the partial replacement of Cs$^+$ with FA$^+$ cations could facilitate the formation of wider quantum wells, which effectively reduced the efficiency roll-off by suppressing Auger recombination [110]. The partial replaced perovskites based LEDs then showed a peak external EQE of 7.8% (Fig. 9j). More importantly, the stability of these perovskites could be substantially improved by the partial substitution while the fabricated LEDs were confirmed to have a longer lifetime of 31 h [110]. Very recently, Tian et al. have found that highly efficient and spectrally stable red LEDs can be realized using $BA_2Cs_{n-1}Pb_nI_{3n+1}$/poly(ethylene oxide) composite thin films as the light emitting layer [111]. The emission peak of the LEDs could be tuned by tuning the value of n. The LED with an emission at 680 nm exhibited a brightness of 1392 cd m^{-2} and an EQE of 6.23%. Also those LEDs showed great operation stability in air, with the electroluminescence dropping about 20% after 4 h of continuous operation.

The performances of 2D perovskites based LEDs are summarized in Table 3. The 2D perovskites already show excellent LED performances, indicating their intriguing potential in practical applications.

5.3. Solar cells

In fact, the recent perovskite fever is induced by the rapid progress in improving their solar cell efficiencies that have been made in a very short period of time [112–115]. Even though great achievements have been achieved, the long term reliability of these perovskite based solar cells is still a big challenge due to the instability of perovskite materials to ambient moisture [113,116]. Current research has found that the 2D RP perovskites were more moisture resistant than the 3D perovskites, which got considerable attention in past years. The recent progresses in 2D RP perovskites based solar cells are summarized in Table 4, which shows the rapid progress in this area.

In 2014, Smith et al. fabricated the first generation of solar cells based on $PEA_2MA_2Pb_3I_{10}$ with a planar device configuration that exhibited an open-circuit voltage of 1.18 V and a PCE of 4.73% (Fig. 10a) [117]. Due to the layered structure of 2D RP perovskites, high-quality films could be easily deposited through spin coating while high-temperature annealing was not required for the subsequent device fabrication. Although the corresponding power conversion efficiency of fabricated cells was far lower than that of $MAPbI_3$ based devices, the 2D RP perovskite cell was more moisture resistant than the one of $MAPbI_3$ [117]. Later, Cao et al. reported another 2D RP perovskite, $BA_2MA_{n-1}Pb_nI_{3n+1}$, based solar cells

Table 3
Typical performance of LEDs based on 2D perovskite.

Material	Wavelength (nm)	FWHM (nm)	Maximum EQE (%)	Maximum current efficiency (cd A^{-1})	Luminescence (cd m^{-2})	Stability	Ref.
PEA$_2$PbBr$_4$	410	14	0.04	–	–	–	[94]
(C$_6$H$_5$CH$_2$NH$_3$)$_2$PbI$_4$	526	15	0.005	–	9	A lifetime of ~1 min	[95]
PEA$_2$MA$_{n-1}$Pb$_n$I$_{3n+1}$ with average $\langle n \rangle = 5$	~740	~50	8.8	–	–	–	[97]
NMA$_2$FAPb$_2$I$_6$Br	763	~50	11.7	–	–	50% after 2 h under operation	[99]
BA$_2$MA$_{n-1}$Pb$_n$Br$_{3n+1}$ with average $\langle n \rangle = 19$	513	~30	9.3	17.1	8000	No degradation after storage for 4 months in N$_2$	[100]
BA$_2$MA$_{n-1}$Pb$_n$I$_{3n+1}$ with average $\langle n \rangle = 19$	748	~50	10.4	0.09	50	No degradation after storage for 8 months in N$_2$	
PEA$_2$FA$_{n-1}$Pb$_n$Br$_{3n+1}$ with average $\langle n \rangle = 3$	532	~25	14.36	62.43	9120	A lifetime of 120 min in dry air with encapsulation	[101]
PEA$_2$MA$_{n-1}$Pb$_n$Br$_{3n+1}$ with average $\langle n \rangle = 5$	526	~20	7.4	~20	8400	50% after 5 min under operation	[104]
OA$_2$MA$_{n-1}$Pb$_n$Br$_{3n+1}$ nanoplatelets	530	20	0.48	–	10,590	Stable in air for at least one week	[105]
OA$_2$MA$_{n-1}$Pb$_n$Br$_{3n+1}$ nanoplatelets with $n = 7-10$	520	~25	2.31	8.1	~1000	–	[106]
PEA$_2$Cs$_{n-1}$Pb$_n$Br$_{3n+1}$ nanoplates	514	17	10.4	31.2	14,000	Stable in glove box for at least one month	[107]
PEA$_2$Cs$_{n-1}$Pb$_n$I$_{3n+1}$ nanoplates	683	34	7.3	–	~100	–	
NMA$_2$CsPb$_2$I$_6$Cl	688	~30	3.7	–	440	50% after 5 h under operation	[108]
NMA$_2$Cs$_{n-1}$Pb$_n$I$_{3n+1}$	694	~30	7.3	–	732	–	[109]
NMA$_2$(FA$_{0.93}$Cs$_{0.07}$)$_{n-1}$Pb$_n$I$_{3n+1}$	783	~50	7.8	–	–	50% after 31 h under operation	[110]
BA$_2$Cs$_{n-1}$Pb$_n$I$_{3n+1}$	680	~50	6.23	1.74	1392	Dropping 20% after 4 h under operation	[111]

[118]. Due to the self-assembly that orients the $[Pb_nI_{3n+1}]^-$ layers perpendicular to the substrate, the obtained 2D perovskite films displayed an ultrahigh surface coverage, benefiting for the utilization in solar cells. The maximum PCE (4.02%) was observed in BA$_2$MA$_{n-1}$Pb$_n$I$_{3n+1}$ based solar cells with a sensitized device structure for $n = 3$ with a short-circuit current density of 9.42 mA cm^2 and an open-circuit voltage of 929 mV. Moreover, the device retained its performance even after the long exposure to a high-humidity environment [118]. However, BA$_2$MA$_2$Pb$_3$I$_{10}$ based solar cells with a planar device structure showed a low short current density with a very low PCE. The authors believed that the electron diffusion length of BA$_2$MA$_2$Pb$_3$I$_{10}$ was very short so that the photogenerated electrons cannot reach the electron transport layer for the carrier collection. Thus, the sensitized device structure with a mesoporous TiO$_2$ was needed to reduce the corresponding transport length of electrons there in order to boost up the cell efficiency.

Besides that, Tsai et al. also attributed the poor PCE of 2D RP perovskites to the inhibition of out-of-plane charge transport by the organic cations, which acted as the insulating spacing layers between the semiconducting inorganic slabs [119]. This way, by the growth of near-single-crystalline quality BA$_2$MA$_3$Pb$_4$I$_{13}$ layered perovskite with a strongly preferential out-of-plane alignment with respect to the contacts (Fig. 10b) in the planar solar cells, it would efficiently facilitate the charge transport; therefore, the PCE of fabricated cells could reach up to 12.52% without hysteresis (Fig. 10c). A hot-casting technique was often used for the synthesis of near-single-crystalline high-quality 2D perovskites films, which showed the much enhanced crystal quality as compared with the room-temperature casting counterparts. The hot-casted films exhibited the substantially larger grains (400 nm) with the much lower density of pinholes in comparison with the room-temperature spin-coated films. In addition, the lack of Urback tails in the optical absorption, the very small Stokes shift, and the strong absorption and photoluminescence were indicative that the hot-casted BA$_2$MA$_3$Pb$_4$I$_{13}$ films behaved like a direct-band gap intrinsic semiconductor with the excellent crystallinity, low trap concentration and little disorder-induced density of states in the band gap. Those features of the hot-casted films were further confirmed with the high PCE of the obtained solar cells. Moreover,

Table 4
Typical performance of the 2D perovskites based solar cells.

| Material	PCE (%)	Open voltage (V)	Short current density (mA cm^{-2})	Filled factor (%)	Stability	Ref.
PEA$_2$MA$_2$Pb$_3$I$_{10}$	4.73	1.18	6.72	60	–	[117]
BA$_2$MA$_2$Pb$_3$I$_{10}$	4.02	0.929	9.42	46	–	[118]
BA$_2$MA$_3$Pb$_4$I$_{13}$	12.52	1.01	16.76	74.13	No degradation over 2250 h with encapsulation under AM1.5G illumination in 64 humidity air	[119]
BA$_2$(MA$_{0.95}$Cs$_{0.05}$)$_3$Pb$_4$I$_{13}$	13.7	1.08	19.95	63.47	10% degradation after 1400 h exposure in 30% humidity air	[120]
BA$_2$(MA$_{0.8}$FA$_{0.2}$)$_3$Pb$_4$I$_{13}$	12.81	0.999	18.12	70.79	12% degradation after 1300 h operation	[121]
(iso-BA)$_2$MA$_3$Pb$_4$I$_{13}$	10.63	1.2	16.64	53.54	–	[122]
PEI$_2$MA$_6$Pb$_7$I$_{22}$	10.08	1.1	13.12	65	5% degradation after 500 h operation	[127]
PEA$_2$MA$_{59}$Pb$_{60}$I$_{181}$	15.36	1.09	19.12	73.7	88.7% degradation after 60 days storage in a low humidity atmosphere	[128]
PEA$_2$MA$_3$Pb$_4$I$_{13}$	12.1	1.16	14.7	71	50% degradation after 1 month storage in 45% humidity air	[130]
PEA$_2$MA$_4$Pb$_5$I$_{16}$/MAPbI$_3$	14.94	1.08	18.63	73	24% degradation after 19 days storage in 75% humidity air	[131]
AVA$_2$PbI$_4$/MAPbI$_3$	14.6	1.025	18.84	75.5	>10,000 h with no degradation under operation	[133]
PEA$_2$MA$_{n-1}$Pb$_n$Br$_{3n+1}$/MAPbI$_3$	19.1	1.08	21.91	80.36	40% degradation after light soaking for 140 h	[134]
FA$_{0.83}$Cs$_{0.17}$Pb(I$_y$Br$_{1-y}$)$_3$	17.5	1.09	22.1	75	20% degradation after 1000 h operation in air	[135]
PEA$_2$FA$_{n-1}$Sn$_n$I$_{3n+1}$	5.05	0.583	14.18	62.14	4% degradation after 100 h storage in a glove box	[141]
PEA$_2$FA$_{n-1}$Sn$_n$I$_{3n+1}$/FASnI$_3$	9.0	0.525	24.1	71	41% degradation after 76 h storage in 20% humidity air	[143]
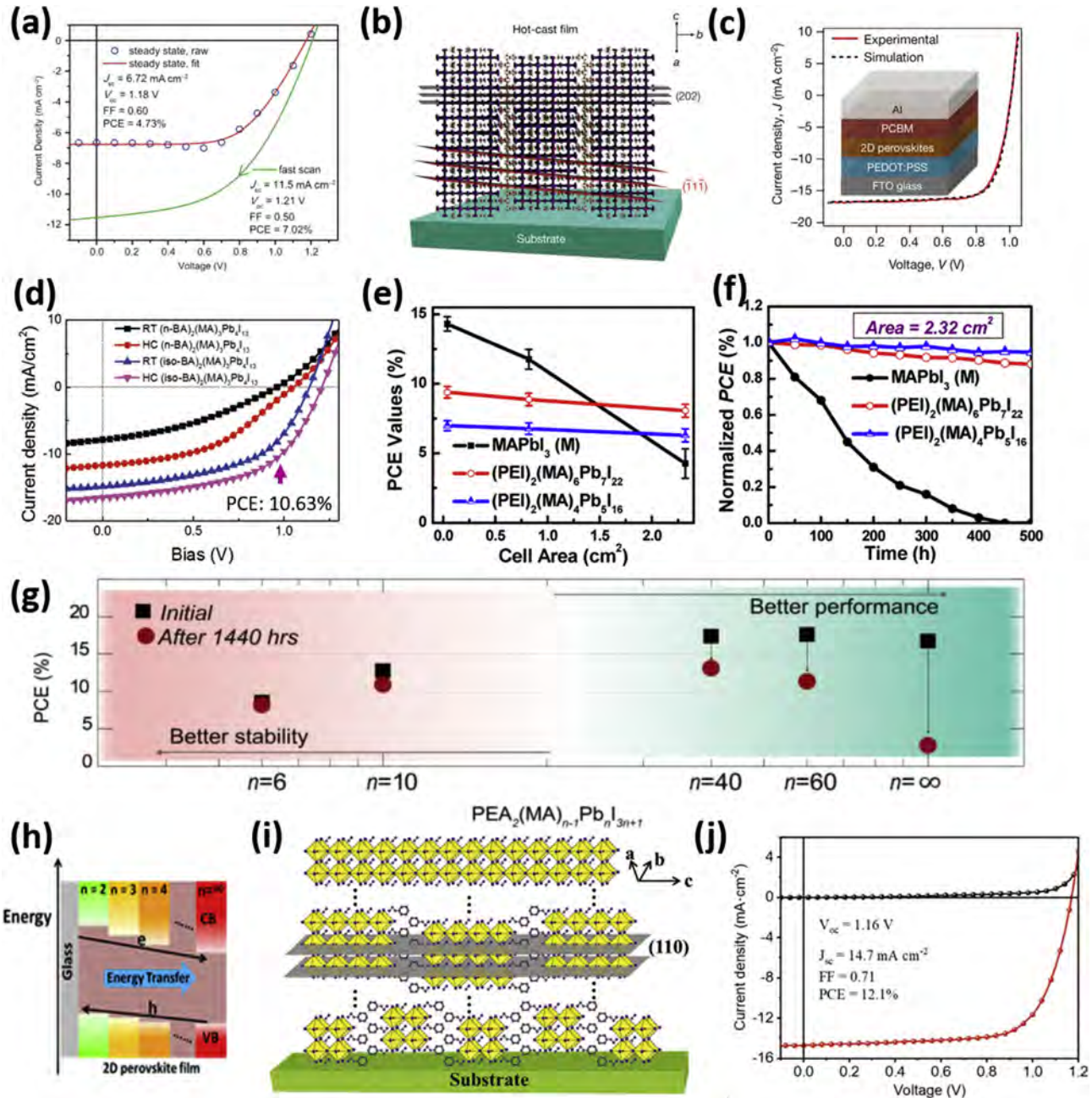
Fig. 10. 2D RP lead perovskite based solar cell structures and performances. (a) Current–voltage curves with the fast scan rate and the steady state for $PEA_2MA_2Pb_3I_{10}$ based solar cell. Reproduced with permission from Ref. [111]. Copyright 2014, WILEY-VCH. (b) Illustrative schematic representation of the (101) orientation, along with the $(\bar{1}\,1\,\bar{1})$ and (2 0 2) planes of a 2D perovskite crystal. (c) Experimental (red line) and simulated (black dashed line) current-density–voltage curves under an AM1.5G solar simulator for planar devices using 2D $BA_2MA_3Pb_4I_{13}$ perovskites as the absorbing layer at the optimized thickness (230 nm). The inset shows the device architecture. (b), (c) Reproduced with permission from Ref. [113]. Copyright 2016, Macmillan Publishers Limited, part of Springer Nature. (d) Representative current density–voltage characteristics of room temperature and hot-cast fabricated (n-BA)$_2MA_3Pb_4I_{13}$ and (iso-BA)$_2MA_3Pb_4I_{13}$ based solar cells under light irradiation of 100 mW cm^{-2} at reverse scan. Reproduced with permission from Ref. [116]. Copyright 2017, WILEY-VCH. (e) Graph shows the corresponding PCE value changes of three materials as the device areas. (f) Stability of unsealed solar cells under simulated solar light (AM1.5, 100 mW cm^{-2}) during a shelf life investigation for 500 h. (e), (f) Reproduced with permission from Ref. [121]. Copyright 2016, American Chemical Society. (g) Solar cell performance as a function of n value based on $PEA_2MA_{n-1}Pb_nI_{3n+1}$. Reproduced with permission from Ref. [122]. Copyright 2016, American Chemical Society. (h) Comparative band gap energy alignment of $BA_2MA_{n-1}Pb_nI_{3n+1}$ perovskites with different n values. Reproduced with permission from Ref. [123]. Copyright 2017, American Chemical Society. (i) Schematic illustration of preferential crystal growth with (1 1 0) plane parallel to the substrate as well as graded multiple 2D RP perovskites. (j) Current density–voltage curves of the champion device under dark and light conditions. (i), (j) Reproduced with permission from Ref. [124]. Copyright 2018, WILEY-VCH.

the unencapsulated layered perovskite devices could retain over 60% of their efficiency over 2250 h under constant, standard (AM1.5G) illumination, and exhibited the much greater tolerance to 65% relative humidity than their 3D equivalents. When the devices were encapsulated, the layered devices did not show any degradation under constant AM1.5G illumination or humidity [119]. All

these results evidently indicated that the crystallinity and orientation of 2D RP perovskites is very important for the performance enhancement of the solar cells. Zhang et al. found that Cs doping in $BA_2MA_3Pb_4I_{13}$ would lead to the perfectly controlled crystal orientation, increased grain size, superior surface quality, reduced trap-state density, enhanced charge-carrier mobility and charge-

transfer kinetics [120]. The fabricated planar solar cells based on the hot-cast prepared Cs (5%) doped 2D RP perovskite showed the enhanced PCE (13.7%) in comparison with the non-doped counterparts. In addition, Cs doping yielded the superior stability for the 2D perovskite solar cells when subjected to high-humidity environment without encapsulation. In particular, the PCE of devices based on 5% doped 2D perovskites was found to only degrade 10% after 1400 h exposure in 30% relative humidity environment, and yield the significantly improved stability under heating and high-moisture environment. Zhou et al. carried out more systematic experiments to understand the principles that linked the crystal orientation to the carrier behavior in polycrystalline films by partial substitution of MA^+ cation with FA^+ cation in $BA_2MA_3Pb_4I_{13}$ [121]. The experimental results revealed that the appropriate FA^+ incorporation can effectively control the perovskite crystallization kinetics, which can increase the quality of polycrystalline films with the increased grain size and limited nonorientated phase, leading to the reduced nonradiative recombination centers. The solar cells with a planar inverted device architecture based on $BA_2(MA_{0.8-}FA_{0.2})_3Pb_4I_{13}$ then showed the enhanced performance with a PCE of 12.81% in comparison with $BA_2MA_3Pb_4I_{13}$ based devices with a PCE of 10.7%. Furthermore, the long term stability of the solar cells were retained with an only 12% drop of PCE after experiencing 1300 h of operation.

Because the organic insulating spacer cations can hinder the charge transport, a shorter spacer cations is preferred in order to enhance the charge transport between layers. Chen et al. found that $(iso-BA)_2MA_3Pb_4I_{13}$, which contained the short branched chain spacer cations $(iso-BA^+)$, showed the remarkable increase in the optical absorption and crystallinity as compared with the conventional linear spacer cations, $n-BA^+$ [122]. By applying a hot-casting technique, the 2D RP perovskites gave the improved light absorption and crystallinity with the excellent ambient stability, which could maintain its initial optical absorption after storage of 840 h in an environmental chamber at room temperature with a relative humidity of 60% without encapsulation, being suitable for practical solar cell utilizations. The highest PCE of the hot-casted 2D RP perovskite based solar cell was found to be 10.63% (Fig. 10d).

In any case, the relatively low charge carrier mobility [122,123] and higher exciton binding energies [40,124,125], and significantly increased band gap [73,126] in 2D RP perovskites may contribute to the origin of low PCE when they are employed for photovoltaics. Because 2D RP perovskites with the larger quantum well width (larger n) would have a smaller band gap with a small excition binding energy, Yao et al. used the multilayered perovskite $PEI_2MA_{n-1}Pb_nI_{3n+1}$ with $n = 3, 5, 7$ acting as the light absorber and these moisture-stable solar cells could achieve a PCE of 10.08% for $PEI_2MA_6Pb_7I_{22}$ for a small size cell (0.04 cm^2) and 8.77% with a large size (2.32 cm^2) (Fig. 10e) [127]. Also, the intercalated polymer ammonium (that is PEI^+), acting as the multiammonium cations, could induce the tight stacking of the separated inorganic unit layers in comparison with BA^+ and PEA^+, leading to the improved charge transfer. Furthermore, the layered perovskite based solar cells yield the high stability with negligible degradation as shown in Fig. 10f. In this case, the protection of the interior perovskite layer from the reaction with water by the hydrophobicity of large polymer cations was thought to be the reason for the enhanced stability to ambient moisture.

As the layer number can drastically affect the performance of corresponding solar cells, it is necessary to carry out systematical investigations on controlling and understanding this effect. Quan et al. carried out recent theoretical and experimental investigations on 2D RP perovskite $PEA_2MA_{n-1}Pb_nI_{3n+1}$ with different n values based planar solar cells [128]. They found that 3D perovskites were marginally stable as they preferred to decompose into PbI_2 and MAI

constituents. The decomposition of 3D perovskite could not start within the bulk spontaneously, in which it needed to initiate from the surface such that the molecules had the sufficient freedom to rearrange. The van der Waals interactions between the capping organic molecules were the key drivers for the increased material stability for 2D RP perovskites because the energy required to remove PEAI from the perovskite was much higher than that for MAI, reducing the desorption rate by 6 orders of magnitude, and slowing the film decomposition in 1000-fold. Both density function theory (DFT) and experimental results showed that the lower n-valued perovskites exhibited the improved stability in comparison with the higher n-values counterparts. Moreover, the quasi-2D RP perovskite films with the higher n values $(n = 40, 60)$ also exhibited the impressive carrier lifetime, carrier mobility and carrier diffusion length, which could be further confirmed with the excellent solar cell performance there. Planar solar cells fabricated with quasi-2D RP perovskites $(n = 60)$ could yield the best performance with a hysteresis-free current-density–voltage curve and a certified AM1.5 PCE of 15.3%. The 2D RP perovskites with the lower n values showed the lower PCE but the high stability, while 2D RP perovskite with the higher n values gave the better performance but the reduced stability. As a result, the 2D RP perovskites with the intermediate n values would have the balance between the stability and cell performance as illustrated in Fig. 10g.

As previously discussed, it is always difficult to synthesize the pure phase 2D RP perovskites, since the obtained 2D RP perovskites are often existed in the mixed phases with different n values. Lately, Liu et al. [129] found a different charge transport picture in the mixed phase 2D RP perovskites in comparison with the previous ones proposed by Wang et al. [99] and Yuan et al. [97]. Specifically, the photo-generated electrons would transfer from the small-n to the large-n phases, while the holes would transfer with an opposite direction as depicted in Fig. 10h. Qing et al. also found this special band alignment and made use of this special feature for solar cells [130]. In particular, they prepared $PEA_2MA_3Pb_4I_{13}$ film and discovered that the mixed phases had the special distribution along the perpendicular direction as shown in Fig. 10i, where the small-n phases preferred to locate at the bottom whereas the large-n phases located at the top of the film. Combined with the special band alignment, the structure was highly beneficial for solar cells due to the efficient charge separation feature. This way, planar solar cells with a champion PCE of 12.1% were achieved in this study (Fig. 10j).

Even though 2D RP perovskites have the good stability, their cell PCE is still far from the satisfactory. In order to make use of both the good stability of 2D RP perovskites and the excellent optoelectronic properties of 3D perovskites, Hu et al. fabricated the hybrid perovskite/perovskite heterojunction solar cells [131]. They used a facile solution-based cation infiltration process to deposit layered perovskite structures onto $MAPbI_3$ film and found the self-assembly of the layered perovskite on top of an intact $MAPbI_3$ layer was accompanied by a reorganization of the perovskite interface (Fig. 11a), which leaded to the enhancement of the open-circuit voltage and PCE. The open-circuit voltage and PCE are found to be 1.08 V and 14.94%, respectively, for the $PEA_2MA_4Pb_5I_{16}/MAPbI_3$ heterostructure, and 1.08 V and 11.49%, respectively, for the $BA_2MA_3Pb_4I_{13}/MAPbI_3$ heterostructure (Fig. 11b). The environmental stability of these heterostructure solar cells could be maintained with the PCE of 11.4% for the $PEA_2MA_4Pb_5I_{16}/MAPbI_3$ heterostructure after exposure to the humid air (75% humidity) for 19 days [131]. The results clearly indicated that the 2D RP perovskite could not only act as the template to rearrange the orientation of the underlying 3D perovskite, but also perform as the moisture barrier to improve the stability of corresponding solar cells.

Also, the template function of 2D RP perovskites is a very unique feature, which showed the powerful ability to further enhance the
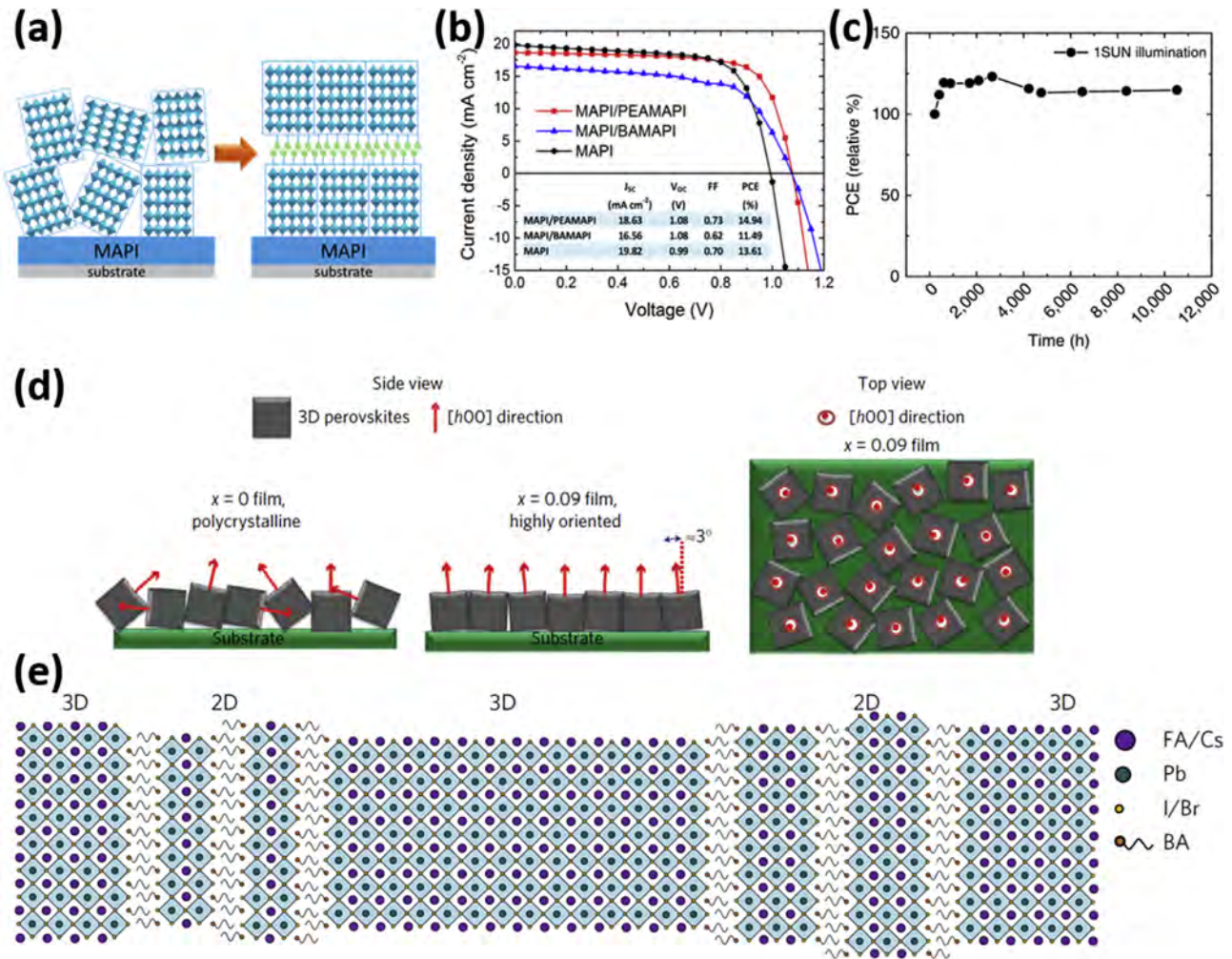
Fig. 11. 2D–3D mixed perovskites. (a) Illustrative schematic interpretation of the surface reorganization of MAPI films upon PEAMAPI formation. (b) Current density–voltage curves and characteristics of the best-performing devices comprising different perovskite layer configurations. (a), (b) Reproduced with permission from Ref. [125]. Copyright 2016, American Chemical Society. (c) Typical module stability test under 1 sun AM1.5G conditions at the stabilized temperature of 55° and at short circuit conditions. Reproduced with permission from Ref. [127]. Copyright 2017, Macmillan Publisher, part of Springer Nature. (d) Illustrative schematic depicting the orientation of 3D perovskite phase in the 9% BA$^+$ ($x = 0.9$) incorporated film, as compared with a low-textured $x = 0$ film, which shows a preference for the [h 0 0] direction to align out-of-plane and no preferential orientation within the plane. (e) Schematic illustration of the proposed self-assembled 2D–3D perovskite film structure. (d), (e) Reproduced with permission from Ref. [129]. Copyright 2017, Macmillan Publisher, part of Springer Nature.

performance of solar cells based on 2D/3D perovskites [132–135]. Grancini et al. found that the 2D/3D AVA$_2$PbI$_4$/MAPbI$_3$ (where AVA is HOOC(CH$_2$)$_4$NH$_3^+$) perovskite with 3% AVA$^+$ would form an exceptional gradually-organized multi-dimensional interface: the 2D perovskite anchored on the oxide network, in templating the growth of a biphasic 3D MAPbI$_3$: an oriented wider band gap phase within the oxide scaffold and a standard tetragonal phase on top of it. This special arrangement then led to a 12.9% PCE in carbon-based architectures, and a 14.6% PEC in standard mesoporous solar cells [133]. More importantly, the solar modules composed of 10 × 10 cm^2 area fabricated by a fully printable industrial-scale process could deliver 11.2% PCE and be stable for more than 10,000 h with zero loss in performances measured under controlled standard conditions (Fig. 11c). In addition, Li et al. developed a low-pressure vapor-assisted solution process to synthesize 2D/3D mixed perovskites [134]. They found that a small addition of PEAI into PbI$_2$ could lead to the formation of a small amount of 2D RP perovskite grains around the MAPbI$_3$ grain to benefit the MAPbI$_3$ grain growth. This way, the sensitized solar cells based on the 2D/3D mixed perovskites showed a champion PCE of 19.1% with a

remarkable fill factor of 80.36% owing to the improved crystallinity of the 3D perovskites. Wang et al. have introduced BA$^+$ cations into a mixed-cation lead mixed-halide FA$_{0.83}$Cs$_{0.17}$Pb(I$_y$Br$_{1-y}$)$_3$ 3D perovskites and observed the formation of 2D perovskite platelets interspersed between the highly orientated 3D perovskite grains [135]. These 3D perovskite would then show a high preference along the [100] direction with the assistance of 2D perovskites (Fig. 11d). Furthermore, the film crystallization was observed to get accelerated in the presence of BA to achieve for the much higher degree of crystallinity while the schematic of self-assembled 2D–3D perovskite film structure is also shown in Fig. 11e. This special structure could also suppress the charge recombination because charges in the 3D grains could be reflected when they reached the 2D–3D interface. Thus, solar cells with an optimal BA content exhibited the average stabilized PCE of 17.5% with a 1.61 eV band gap perovskite and 15.8% with a 1.72 eV band gap perovskite. Notably, solar cells could sustain 80% of their efficiency after 1000 h operation in air, and close to 4000 h operation when encapsulated.

Because lead-based perovskites are potentially environmentally toxic, they are subject to the international waste disposal regulation

[136]. For 3D perovskites, Sn and Ge have been explored to replace Pb [136−138]. However, the oxidation of Sn^{2+}/Ge^{2+} to the higher valance and the consequent formation of Sn/Ge lattice vacancies are still the big challenge [137]. Experiments have shown that 2D Sn based perovskites possessed the much enhanced properties as compared with the 3D counterparts [139,140]. For instance, Liao et al. carried out investigations on the performance of Sn 2D perovskites based solar cells [141]. By using the appropriate ratio (20%) of PEA to FA as encapsulating molecules, the highly orientated growth of 2D $PEA_2FA_{n-1}Sn_nI_{3n+1}$ perovskite films on nickel oxide substrates was realized, leading to the greatly improved air stability in comparison with $FASnI_3$. The 2D perovskite films mainly contained the $PEA_2FA_8Sn_9I_{28}$ phase with a preferential orientation of $(1\,0\,\bar{1})$, where the layer plane was perpendicular to the substrate as shown in Fig. 12a. The perpendicular orientation growth of the perovskite would facilitate the growth of compact and smooth films (Fig. 12b), which was beneficial for protecting the film from oxygen infiltration and promising for the fabrication of planar solar cells. This way, the inverted planar solar cells based on the perovskite films showed an average PCE of 5.05% (Fig. 12c). The PCE could

retain 96% of its initial value for over 100 h in the N_2 atmosphere glove box, indicating its good stability (Fig. 12d). Simultaneously, Cao et al. reported the pure phase $BA_2MA_2Sn_3I_{10}$ and $BA_2MA_3Sn_4I_{13}$ based solar cells [142]. Due to the short carrier lifetimes of $BA_2MA_2Sn_3I_{10}$ and $BA_2MA_3Sn_4I_{13}$ films, mesoporous TiO_2 was utilized as the electron-accepting layer to facilitate the collection of photogenerated charge carriers. Although the solar cells showed the enhanced stability (Fig. 12e), the obtained PCEs are still low, being 1.94% for $BA_2MA_2Sn_3I_{10}$ and 2.53% for $BA_2MA_3Sn_4I_{13}$.

In any case, the mixed 2D−3D perovskites were found to improve the performance of Sn-based perovskite solar cells [143,144]. Shao et al. observed that the addition of a very small amount of layered tin perovskite in 3D tin perovskite would induce the superior crystallinity and a well-defined orientation of the 3D $FASnI_3$ grains (Fig. 12f and g) [143], being similar to the Pb-based 2D−3D perovskites [135]. The high degree of crystallinity and the preferential crystal orientation were fundamental for the improvement of solar cell performance. This way, the 2D−3D Sn perovskites based solar cell showed a PCE as high as 9% in a p-i-n planar device structure with negligible hysteresis (Fig. 12h).
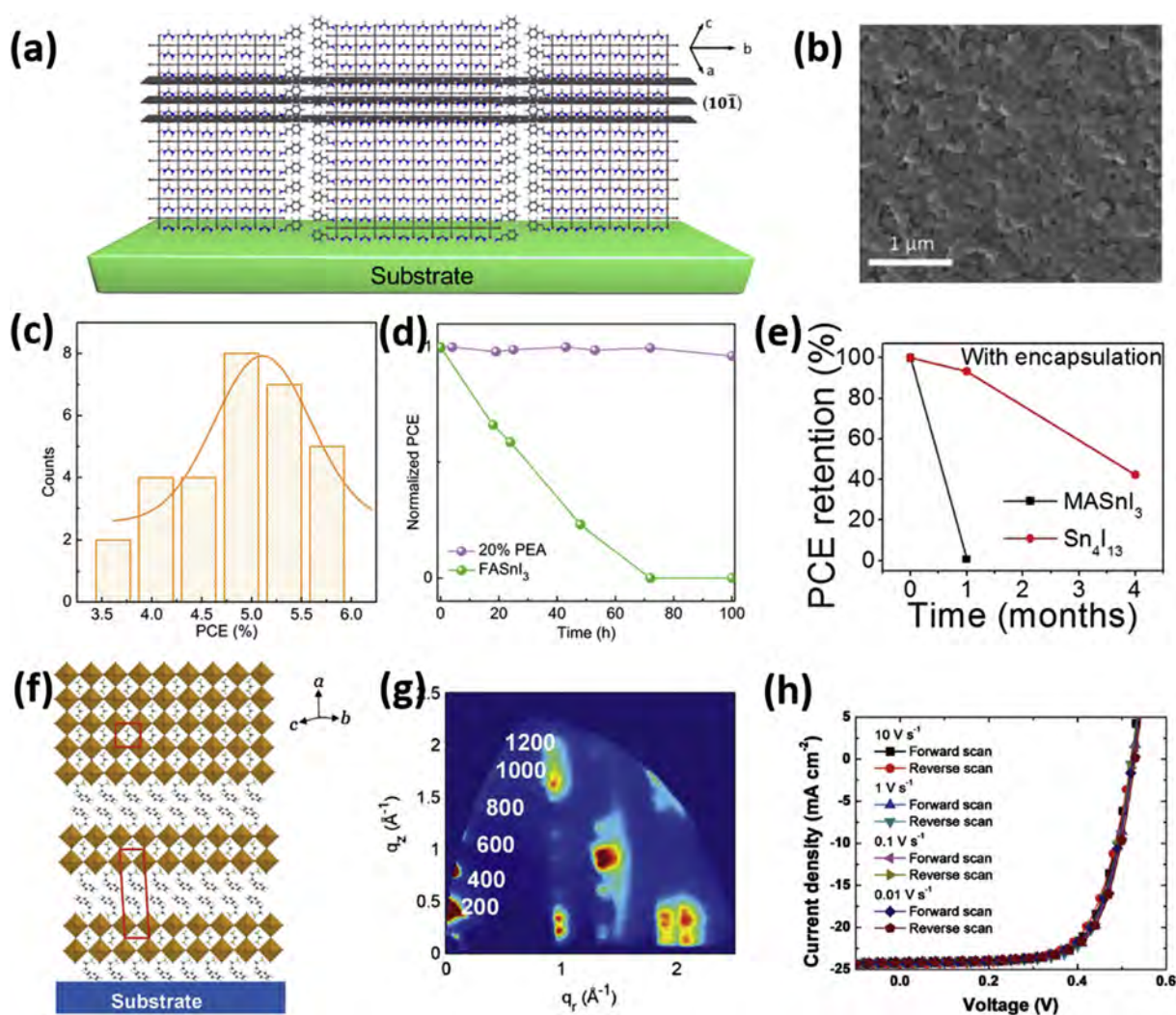

Fig. 12. Sn-based 2D RP perovskites based solar cells. (a) Schematic illustration of the $(1\,0\,1)$ plane of a $PEA_2FA_8Sn_9I_{28}$ 2D perovskite crystal. (b) SEM image of the 2D perovskite film. (c) Statistics of the PCE distribution. Orange solid line denotes the Gaussian distribution fitting. (d) Normalized PCE of the unencapsulated device based on $FASnI_3$ and 20% PEA-doped perovskite film stored in a glove box for over 100 h. (a)–(d) Reproduced with permission from Ref. [134]. Copyright 2017, American Chemical Society. (e) PCE retention of an encapsulated layered Sn-perovskite solar cell after several months. Reproduced with permission from Ref. [135]. Copyright 2017, American Chemical Society. (f) Schematic of the 2D−3D mixture with the orientation of $(1\,0\,0)$. (g) Grazing incidence wide-angle X-ray scattering of the 2D−3D mixture film. (h) Forward and reverse sweeps of the current density versus voltage of the 2D−3D perovskite cell measured at different rates. (f)–(h) Reproduced with permission from Ref. [136]. Copyright 2018, WILEY-VCH.

6. Outlook

In this work, we have summarized the recent progresses that have been made in the synthesis of 2D perovskites, evaluation of their interesting optoelectronic properties, and related energy applications. From the above discussions, many new opportunities are ahead of us in this promising area. Although great achievements have been done for various 2D perovskite materials, there are still many challenges and opportunities for the practical utilization of 2D perovskites.

(1) Stability

Despite 2D perovskites, especially the 2D RP perovskites, are found to be more stable than 3D perovskites, the fabricated devices still encounter durability issues. More works are required to first understand their degradation mechanisms and then to come up with simple methods to improve their stability.

(2) Synthesis of 2D perovskite single crystals with the large dimension and controlled thickness

As we discussed for photodetectors, single crystals with large lateral dimension is highly preferred. High performance photodetectors are relied on the high quality of the materials. However, until now, the controllable synthesis of large-scale 2D perovskite single crystals are not yet achieved. In this case, the synthesis methods need to be developed, modified or further optimized for the realization of atomically thin 2D perovskites with dimension up to 100 μm or larger.

(3) Opportunities in photodetectors

As has been demonstrated that the 2D RP perovskites with small n (<4) tend to orient parallel to the substrate, whereas large n tend to preferentially orient normal to it [119]. This special property has been utilized in high performance solar cells. In photodetectors, it does not explored yet. Due to the vertical alignment of the inorganic semiconductor layer of the 2D RP perovskites, it is possible to realize high performance photodetectors using vertical device structure, where electrodes can directly in contact with the semiconductor layer, not the insulating organic layer. Two advantage of the structure can be anticipated: a, good contact; b, efficiency carrier transport. Furthermore, the large n value 2D RP perovskites have small exciton binding energy, which can be more easily dissociate by external electrical field. This way, high performance photodetectors can be possible. For small n, the contact problem has not been investigated systematically.

As has demonstrated the high performance of mixed-n 2D RP perovskite LEDs and solar cells depends on the charge transport between different n 2D RP perovskite. This special charge transport, though the detailed transport mechanism is still in controversial, can be utilized in high performance photodetectors due to the automatic electron−hole pairs separation in mixed-n 2D RP perovskite.

(4) Opportunities in LEDs

LEDs based on mixed-n 2D RP perovskites always show high performance, such as high EQE, high luminescence. The performance of the LEDs is also affected by the long chain capping layers. How does the performance of the LEDs affect by the long chain capping layers is still unknown. Further investigation are needed to clarify it. As the composition and orientation of the mixed-n 2D RP perovskites are largely affected by synthesizing condition [145], it is necessary to explore those effect on the performance of LEDs.

(5) Opportunities in solar cells

The performance of 2D RP solar cells is affected by many factors, such as the properties of active layer 2D RP perovskite, hole transport layer, electron transport layer, and/or scaffold, etc., which make it complicated but provide many opportunities to enhance the performance. Also, appropriate protecting layer is needed to make the long time operation reliable. Still, like the cast in LEDs, the performance of solar cells also affected by the long chain capping layers. The exact mechanism of the capping layers on the performance needs further investigation.

(6) Other possible applications

Recently, self-powered flexible photodetectors become a hot topic because of the high demands in portable devices [146]. Bulk MAPbI$_3$ showed excellence performance when fabricated as self-powered flexible photodetector [147]. 2D perovskites have already shown potential in flexible photodetectors. This way, it is possible to develop 2D perovskites based self-powered flexible photodetectors.

Bulk perovskites, such as MAPbI$_3$ [148] and MAPbBr$_3$ [149], show large photostriction, which is promising for applications in microsensing and microactuation. The large photostriction possibly arises from the weakening of the hydrogen bonding between N and X (X = Br, I) by the photo-generated carriers [148]. Because of the similar crystal structure of 2D RP perovskites with conventional perovskites, it is possible to observe large photostriction in 2D RP perovskites, which needs exploration.

MAPbI$_3$ showed saturated light absorption character, which is utilized in mode lock fiber lasers [150]. Considering the similar physical properties, 2D RP perovskites may find application in mode-lock lasers.

In summary, 2D perovskites are demonstrated with many exciting optoelectronic properties, which are advantageous for many energy applications, such as highly efficient photodetectors, LEDs and photovoltaic devices. In this regard, much progress towards the controllable synthesis of 2D perovskites, exploration of novel properties and new mechanisms as well as the realization of high-performance 2D perovskite optoelectronic devices is anticipated in the near future.

Appendix A. Supplementary data

Supplementary data to this article can be found online at https://doi.org/10.1016/j.mtener.2018.10.008.

References

[1] A. Kojima, K. Teshima, Y. Shirai, T. Miyasaka, Organometal halide perovskites as visible-light sensitizers for photovoltaic cells, J. Am. Chem. Soc. 131 (2009) 6050−6051, https://doi.org/10.1021/ja809598r.

[2] J.-P. Correa-Baena, A. Abate, M. Saliba, W. Tress, T.J. Jacobsson, M. Grätzel, A. Hagfeldt, The rapid evolution of highly efficient perovskite solar cells,

Energy Environ. Sci. 10 (2017) 710–727, https://doi.org/10.1039/C6EE03397K.

[3] S. De Wolf, J. Holovsky, S.-J. Moon, P. Löper, B. Niesen, M. Ledinsky, F.-J. Haug, J.-H. Yum, C. Ballif, Organometallic halide perovskites: sharp optical absorption edge and its relation to photovoltaic performance, J. Phys. Chem. Lett. 5 (2014) 1035–1039, https://doi.org/10.1021/jz500279b.

[4] W.J. Yin, T. Shi, Y. Yan, Unique properties of halide perovskites as possible origins of the superior solar cell performance, Adv. Mater. 26 (2014) 4653–4658, https://doi.org/10.1002/adma.201306281.

[5] C. Wehrenfennig, G.E. Eperon, M.B. Johnston, H.J. Snaith, L.M. Herz, High charge carrier mobilities and lifetimes in organolead trihalide perovskites, Adv. Mater. 26 (2014) 1584–1589, https://doi.org/10.1002/adma.201305172.

[6] T. Leijtens, S.D. Stranks, G.E. Eperon, R. Lindblad, E.M. Johansson, I.J. McPherson, H. Rensmo, J.M. Ball, M.M. Lee, H.J. Snaith, Electronic properties of meso-superstructured and planar organomineral halide perovskite films: charge trapping, photodoping, and carrier mobility, ACS Nano 8 (2014) 7147–7155, https://doi.org/10.1021/nn502115k.

[7] C. Motta, F. El-Mellouhi, S. Sanvito, Charge carrier mobility in hybrid halide perovskites, Sci. Rep. 5 (2015) 12746, https://doi.org/10.1038/srep12746.

[8] A.A. Zhumekenov, M.I. Saidaminov, M.A. Haque, E. Alarousu, S.P. Sarmah, B. Murali, I. Dursun, X.-H. Miao, A.L. Abdelhady, T. Wu, O.F. Mohammed, O.M. Bakr, Formamidinium lead halide perovskite crystals with unprecedented long carrier dynamics and diffusion length, ACS Energy Lett. 1 (2016) 32–37, https://doi.org/10.1021/acsenergylett.6b00002.

[9] G.R. Yettapu, D. Talukdar, S. Sarkar, A. Swarnkar, A. Nag, P. Ghosh, P. Mandal, Terahertz conductivity within colloidal CsPbBr$_3$ perovskite nanocrystals: remarkably high carrier mobilities and large diffusion lengths, Nano Lett. 16 (2016) 4838–4848, https://doi.org/10.1021/acs.nanolett.6b01168.

[10] Q. Dong, Y. Fang, Y. Shao, P. Mulligan, J. Qiu, L. Cao, J. Huang, Electron–hole diffusion lengths > 175 μm in solution-grown CH$_3$NH$_3$PbI$_3$ single crystals, Science 347 (2015) 967–970, https://doi.org/10.1126/science.aaa5760.

[11] D. Shi, V. Adinolfi, R. Comin, M. Yuan, E. Alarousu, A. Buin, Y. Chen, S. Hoogland, A. Rothenberger, K. Katsiev, Y. Losovyj, X. Zhang, P.A. Dowben, O.F. Mohammed, E.H. Sargent, O.M. Bakr, Low trap-state density and long carrier diffusion in organolead trihalide perovskite single crystals, Science 347 (2015) 519–522, https://doi.org/10.1126/science.aaa2725.

[12] S.D. Stranks, G.E. Eperon, G. Grancini, C. Menelaou, M.J. Alcocer, T. Leijtens, L.M. Herz, A. Petrozza, H.J. Snaith, Electron–hole diffusion lengths exceeding 1 micrometer in an organometal trihalide perovskite absorber, Science 342 (2013) 341–344, https://doi.org/10.1126/science.1243982.

[13] G. Xing, N. Mathews, S. Sun, S.S. Lim, Y.M. Lam, M. Grätzel, S. Mhaisalkar, T.C. Sum, Long-range balanced electron- and hole-transport lengths in organic–inorganic CH$_3$NH$_3$PbI$_3$, Science 342 (2013) 344–347, https://doi.org/10.1126/science.1243167.

[14] A. Miyata, A. Mitioglu, P. Plochocka, O. Portugall, J.T.-W. Wang, S.D. Stranks, H.J. Snaith, R.J. Nicholas, Direct measurement of the exciton binding energy and effective masses for charge carriers in organic–inorganic tri-halide perovskites, Nat. Phys. 11 (2015) 582–587, https://doi.org/10.1038/nphys3357.

[15] J. Even, L. Pedesseau, C. Katan, Analysis of multivalley and multibandgap absorption and enhancement of free carriers related to exciton screening in hybrid perovskites, J. Phys. Chem. C 118 (2014) 11566–11572, https://doi.org/10.1021/jp503337a.

[16] Y. Zhao, K. Zhu, Organic–inorganic hybrid lead halide perovskites for optoelectronic and electronic applications, Chem. Soc. Rev. 45 (2016) 655–689, https://doi.org/10.1039/C4CS00458B.

[17] T.M. Brenner, D.A. Egger, L. Kronik, G. Hodes, D. Cahen, Hybrid organic—inorganic perovskites: low-cost semiconductors with intriguing charge-transport properties, Nat. Rev. Mater. 1 (2016) 15007, https://doi.org/10.1038/natrevmats.2015.7.

[18] S.P. Senanayak, B. Yang, T.H. Thomas, N. Giesbrecht, W. Huang, E. Gann, B. Nair, K. Goedel, S. Guha, X. Moya, C.R. McNeill, P. Docampo, A. Sadhanala, R.H. Friend, H. Sirringhaus, Understanding charge transport in lead iodide perovskite thin-film field-effect transistors, Sci. Adv. 3 (2017) e1601935, https://doi.org/10.1126/sciadv.1601935.

[19] Y.H. Lin, P. Pattanasattayavong, T.D. Anthopoulos, Metal-halide perovskite transistors for printed electronics: challenges and opportunities, Adv. Mater. 29 (2017) 1702838, https://doi.org/10.1002/adma.201702838.

[20] D. Li, H.C. Cheng, Y. Wang, Z. Zhao, G. Wang, H. Wu, Q. He, Y. Huang, X. Duan, The effect of thermal annealing on charge transport in organolead halide perovskite microplate field-effect transistors, Adv. Mater. 29 (2017) 1601959, https://doi.org/10.1002/adma.201601959.

[21] X. Hu, X. Zhang, L. Liang, J. Bao, S. Li, W. Yang, Y. Xie, High-performance flexible broadband photodetector based on organolead halide perovskite, Adv. Funct. Mater. 24 (2014) 7373–7380, https://doi.org/10.1002/adfm.201402020.

[22] C. Lan, R. Dong, Z. Zhou, L. Shu, D. Li, S. Yip, J.C. Ho, Large-scale synthesis of freestanding layer-structured PbI$_2$ and MAPbI$_3$ nanosheets for high-performance photodetection, Adv. Mater. 29 (2017) 1702759, https://doi.org/10.1002/adma.201702759.

[23] P. Wangyang, C. Gong, G. Rao, K. Hu, X. Wang, C. Yan, L. Dai, C. Wu, J. Xiong, Recent advances in halide perovskite photodetectors based on different dimensional materials, Adv. Opt. Mater. 6 (2018) 1701302, https://doi.org/10.1002/adom.201701302.

[24] L. Ji, H.-Y. Hsu, J. Lee, A.J. Bard, E.T. Yu, High performance photodetectors based on solution-processed epitaxial grown hybrid halide perovskites,

[25] Nano Lett. 18 (2018) 994–1000, https://doi.org/10.1021/acs.nanolett.7b04445.

A.B. Wong, M. Lai, S.W. Eaton, Y. Yu, E. Lin, L. Dou, A. Fu, P. Yang, Growth and anion exchange conversion of CH$_3$NH$_3$PbX$_3$ nanorod arrays for light-emitting diodes, Nano Lett. 15 (2015) 5519–5524, https://doi.org/10.1021/acs.nanolett.5b02082.

[26] M.R. Leyden, L. Meng, Y. Jiang, L.K. Ono, L. Qiu, E.J. Juarez-Perez, C. Qin, C. Adachi, Y. Qi, Methylammonium lead bromide perovskite light-emitting diodes by chemical vapor deposition, J. Phys. Chem. Lett. 8 (2017) 3193–3198, https://doi.org/10.1021/acs.jpclett.7b01093.

[27] S. Yuan, Z.-K. Wang, M.-P. Zhuo, Q. Tian, Y. Jin, L.-S. Liao, Self-assembled high quality CsPbBr$_3$ quantum dot films toward highly efficient light-emitting diodes, ACS Nano 12 (2018) 9541–9548, https://doi.org/10.1021/acsnano.8b05185.

[28] W. Choi, N. Choudhary, G.H. Han, J. Park, D. Akinwande, Y.H. Lee, Recent development of two-dimensional transition metal dichalcogenides and their applications, Mater. Today 20 (2017) 116–130, https://doi.org/10.1016/j.mattod.2016.10.002.

[29] D.L. Duong, S.J. Yun, Y.H. Lee, van der Waals layered materials: opportunities and challenges, ACS Nano 11 (2017) 11803–11830, https://doi.org/10.1021/acsnano.7b07436.

[30] L. Polavarapu, B. Nickel, J. Feldmann, A.S. Urban, Advances in quantum-confined perovskite nanocrystals for optoelectronics, Adv. Energy Mater. 7 (2017) 1700267, https://doi.org/10.1002/aenm.201700267.

[31] K. Hong, Q. Van Le, S.Y. Kim, H.W. Jang, Low-dimensional halide perovskites: review and issues, J. Mater. Chem. C 6 (2018) 2189–2209, https://doi.org/10.1039/C7TC05658C.

[32] J. Jagielski, S. Kumar, W.-Y. Yu, C.-J. Shih, Layer-controlled two-dimensional perovskites: synthesis and optoelectronics, J. Mater. Chem. C 5 (2017) 5610–5627, https://doi.org/10.1039/C7TC00538E.

[33] S. Chen, G. Shi, Two-dimensional materials for halide perovskite-based optoelectronic devices, Adv. Mater. 29 (2017) 1600018, https://doi.org/10.1002/adma.201605448.

[34] C. Huo, B. Cai, Z. Yuan, B. Ma, H. Zeng, Two-dimensional metal halide perovskites: theory, synthesis, and optoelectronics, Small Methods 1 (2017) 1600018, https://doi.org/10.1002/smtd.201600018.

[35] Y. Chen, Y. Sun, J. Peng, J. Tang, K. Zheng, Z. Liang, 2D Ruddlesden–Popper perovskites for optoelectronics, Adv. Mater. 30 (2018) 1703487, https://doi.org/10.1002/adma.201703487.

[36] L. Dou, Emerging two-dimensional halide perovskite nanomaterials, J. Mater. Chem. C 5 (2017) 11165–11173, https://doi.org/10.1039/C7TC02863F.

[37] E. Shi, Y. Gao, B.P. Finkenauer, A.H. Coffey, L. Dou, Two-dimensional halide perovskite nanomaterials and heterostructures, Chem. Soc. Rev. 47 (2018) 6046–6072, https://doi.org/10.1039/C7CS00886D.

[38] G. Kieslich, S. Sun, A.K. Cheetham, Solid-state principles applied to organic–inorganic perovskites: new tricks for an old dog, Chem. Sci. 5 (2014) 4712–4715, https://doi.org/10.1039/C4SC02211D.

[39] B. Saparov, D.B. Mitzi, Organic–inorganic perovskites: structural versatility for functional materials design, Chem. Rev. 116 (2016) 4558–4596, https://doi.org/10.1021/acs.chemrev.5b00715.

[40] H. Lin, C. Zhou, Y. Tian, T. Siegrist, B. Ma, Low-dimensional organometal halide perovskites, ACS Energy Lett. 3 (2017) 54–62, https://doi.org/10.1021/acsenergylett.7b00926.

[41] C. Tan, X. Cao, X.-J. Wu, Q. He, J. Yang, X. Zhang, J. Chen, W. Zhao, S. Han, G.-H. Nam, M. Sindoro, H. Zhang, Recent advances in ultrathin two-dimensional nanomaterials, Chem. Rev. 117 (2017) 6225–6331, https://doi.org/10.1021/acs.chemrev.6b00558.

[42] M. Zhong, S. Zhang, L. Huang, J. You, Z. Wei, X. Liu, J. Li, Large-scale 2D PbI$_2$ monolayers: experimental realization and their indirect band-gap related properties, Nanoscale 9 (2017) 3736–3741, https://doi.org/10.1039/C6NR07924E.

[43] S.T. Ha, X. Liu, Q. Zhang, D. Giovanni, T.C. Sum, Q. Xiong, Synthesis of organic–inorganic lead halide perovskite nanoplatelets: towards high-performance perovskite solar cells and optoelectronic devices, Adv. Opt. Mater. 2 (2014) 838–844, https://doi.org/10.1002/adom.201400106.

[44] L. Niu, Q. Zeng, J. Shi, C. Cong, C. Wu, F. Liu, J. Zhou, W. Fu, Q. Fu, C. Jin, T. Yu, X. Liu, Z. Liu, Controlled growth and reliable thickness-dependent properties of organic–inorganic perovskite platelet crystal, Adv. Funct. Mater. 26 (2016) 5263–5270, https://doi.org/10.1002/adfm.201601392.

[45] J. Liu, Y. Xue, Z. Wang, Z.-Q. Xu, C. Zheng, B. Weber, J. Song, Y. Wang, Y. Lu, Y. Zhang, Q. Bao, Two-dimensional CH$_3$NH$_3$PbI$_3$ perovskite: synthesis and optoelectronic application, ACS Nano 10 (2016) 3536–3542, https://doi.org/10.1021/acsnano.5b07791.

[46] G. Wang, D. Li, H.-C. Cheng, Y. Li, C.-Y. Chen, A. Yin, Z. Zhao, Z. Lin, H. Wu, Q. He, M. Ding, Y. Liu, Y. Huang, X. Duan, Wafer-scale growth of large arrays of perovskite microplate crystals for functional electronics and optoelectronics, Sci. Adv. 1 (2015) e1500613, https://doi.org/10.1126/sciadv.1500613.

[47] Y. Wang, Y. Shi, G. Xin, J. Lian, J. Shi, Two-dimensional van der Waals epitaxy kinetics in a three-dimensional perovskite halide, Cryst. Growth Des. 15 (2015) 4741–4749, https://doi.org/10.1021/acs.cgd.5b00949.

[48] W. Niu, A. Eiden, G. Vijaya Prakash, J.J. Baumberg, Exfoliation of self-assembled 2D organic–inorganic perovskite semiconductors, Appl. Phys. Lett. 104 (2014) 171111, https://doi.org/10.1063/1.4874846.

[49] J.-C. Blancon, H. Tsai, W. Nie, C.C. Stoumpos, L. Pedessau, C. Katan, M. Kepenekian, C.M.M. Soe, K. Appavoo, M.Y. Sfeir, S. Tretiak, P.M. Ajayan,

M.G. Kanatzidis, J. Even, J.J. Crochet, A.D. Mohite, Extremely efficient internal exciton dissociation through edge states in layered 2D perovskites, Science 355 (2017) 1288–1292, https://doi.org/10.1126/science.aal4211.

[50] O. Yaffe, A. Chernikov, Z.M. Norman, Y. Zhong, A. Velauthapillai, A. van Der Zande, J.S. Owen, T.F. Heinz, Excitons in ultrathin organic–inorganic perovskite crystals, Phys. Rev. B 92 (2015) 045414, https://doi.org/10.1103/PhysRevB.92.045414.

[51] L. Dou, A.B. Wong, Y. Yu, M. Lai, N. Kornienko, S.W. Eaton, A. Fu, C.G. Bischak, J. Ma, T. Ding, N.S. Ginsberg, L.-W. Wang, A.P. Alivisatos, P. Yang, Atomically thin two-dimensional organic–inorganic hybrid perovskites, Science 349 (2015) 1518–1521, https://doi.org/10.1126/science.aac7660.

[52] J. Chen, L. Gan, F. Zhuge, H. Li, J. Song, H. Zeng, T. Zhai, A ternary solvent method for large-sized two-dimensional perovskites, Angew. Chem. Int. Ed. 56 (2017) 2390–2394, https://doi.org/10.1002/anie.201611794.

[53] J. Chen, Y. Wang, L. Gan, Y. He, H. Li, T. Zhai, Generalized self-doping engineering towards ultrathin and large-sized two-dimensional homologous perovskites, Angew. Chem. Int. Ed. 56 (2017) 14893–14897, https://doi.org/10.1002/anie.201708434.

[54] Q. Zhang, L. Chu, F. Zhou, W. Ji, G. Eda, Excitonic properties of chemically synthesized 2D organic–inorganic hybrid perovskite nanosheets, Adv. Mater. 30 (2018) 1704055, https://doi.org/10.1002/adma.201704055.

[55] S. Yang, W. Niu, A.L. Wang, Z. Fan, B. Chen, C. Tan, Q. Lu, H. Zhang, Ultrathin two-dimensional organic–inorganic hybrid perovskite nanosheets with bright, tunable photoluminescence and high stability, Angew. Chem. Int. Ed. 56 (2017) 4252–4255, https://doi.org/10.1002/anie.201701134.

[56] Y.H. Lee, X.Q. Zhang, W. Zhang, M.T. Chang, C.T. Lin, K.D. Chang, Y.C. Yu, J.T.W. Wang, C.S. Chang, L.J. Li, T.-W. Lin, Synthesis of large-area MoS2 atomic layers with chemical vapor deposition, Adv. Mater. 24 (2012) 2320–2325, https://doi.org/10.1002/adma.201104798.

[57] C. Lan, Z. Zhou, Z. Zhou, C. Li, L. Shu, L. Shen, D. Li, R. Dong, S. Yip, J.C. Ho, Wafer-scale synthesis of monolayer WS2 for high-performance flexible photodetectors by enhanced chemical vapor deposition, Nano Res. 11 (2018) 3371–3384, https://doi.org/10.1007/s12274-017-1941-4.

[58] Z. Chen, Y. Wang, X. Sun, Y. Guo, Y. Hu, E. Wertz, X. Wang, H. Gao, T.M. Lu, J. Shi, van der Waals hybrid perovskite of high optical quality by chemical vapor deposition, Adv. Opt. Mater. 5 (2017) 1700373, https://doi.org/10.1002/adom.201700373.

[59] V.A. Hintermayr, A.F. Richter, F. Ehrat, M. Döblinger, W. Vanderlinden, J.A. Sichert, Y. Tong, L. Polavarapu, J. Feldmann, A.S. Urban, Tuning the optical properties of perovskite nanoplatelets through composition and thickness by ligand-assisted exfoliation, Adv. Mater. 28 (2016) 9478–9485, https://doi.org/10.1002/adma.201602897.

[60] Q.A. Akkerman, S.G. Motti, A.R. Srimath Kandada, E. Mosconi, V. D'Innocenzo, G. Bertoni, S. Marras, B.A. Kamino, L. Miranda, F. De Angelis, A. Petrozza, M. Prato, L. Manna, Solution synthesis approach to colloidal cesium lead halide perovskite nanoplatelets with monolayer-level thickness control, J. Am. Chem. Soc. 138 (2016) 1010–1016, https://doi.org/10.1021/jacs.5b12124.

[61] Y. Bekenstein, B.A. Koscher, S.W. Eaton, P. Yang, A.P. Alivisatos, Highly luminescent colloidal nanoplates of perovskite cesium lead halide and their oriented assemblies, J. Am. Chem. Soc. 137 (2015) 16008–16011, https://doi.org/10.1021/jacs.5b11199.

[62] L. Lv, Y. Xu, H. Fang, W. Luo, F. Xu, L. Liu, B. Wang, X. Zhang, D. Yang, W. Hu, A. Dong, Generalized colloidal synthesis of high-quality, two-dimensional cesium lead halide perovskite nanosheets and their applications in photodetectors, Nanoscale 8 (2016) 13589–13596, https://doi.org/10.1039/C6NR03428D.

[63] J. Song, L. Xu, J. Li, J. Xue, Y. Dong, X. Li, H. Zeng, Monolayer and few-layer all-inorganic perovskites as a new family of two-dimensional semiconductors for printable optoelectronic devices, Adv. Mater. 28 (2016) 4861–4869, https://doi.org/10.1002/adma.201600225.

[64] J. Shamsi, Z. Dang, P. Bianchini, C. Canale, F. Di Stasio, R. Brescia, M. Prato, L. Manna, Colloidal synthesis of quantum confined single crystal CsPbBr3 nanosheets with lateral size control up to the micrometer range, J. Am. Chem. Soc. 138 (2016) 7240–7243, https://doi.org/10.1021/jacs.6b03166.

[65] Q. Zhang, R. Su, X. Liu, J. Xing, T.C. Sum, Q. Xiong, High-quality whispering-gallery-mode lasing from cesium lead halide perovskite nanoplatelets, Adv. Funct. Mater. 26 (2016) 6238–6245, https://doi.org/10.1002/adfm.201601690.

[66] Z. Ye, T. Cao, K. O'Brien, H. Zhu, X. Yin, Y. Wang, S.G. Louie, X. Zhang, Probing excitonic dark states in single-layer tungsten disulphide, Nature 513 (2014) 214, https://doi.org/10.1038/nature13734.

[67] X. Hong, T. Ishihara, A. Nurmikko, Dielectric confinement effect on excitons in PbI4-based layered semiconductors, Phys. Rev. B 45 (1992) 6961, https://doi.org/10.1103/PhysRevB.45.6961.

[68] T. Ishihara, Optical properties of PbI-based perovskite structures, J. Lumin. 60 (1994) 269–274, https://doi.org/10.1016/0022-2313(94)90145-7.

[69] T. Ishihara, J. Takahashi, T. Goto, Exciton state in two-dimensional perovskite semiconductor (C10H21NH3)2PbI4, Solid State Commun. 69 (1989) 933–936, https://doi.org/10.1016/0038-1098(89)90935-6.

[70] T. Ishihara, J. Takahashi, T. Goto, Optical properties due to electronic transitions in two-dimensional semiconductors (CnH2n+1NH3)2PbI4, Phys. Rev. B 42 (1990) 11099, https://doi.org/10.1103/PhysRevB.42.11099.

[71] E. Muljarov, S. Tikhodeev, N. Gippius, T. Ishihara, Excitons in self-organized semiconductor/insulator superlattices: PbI-based perovskite compounds, Phys. Rev. B 51 (1995) 14370, https://doi.org/10.1103/PhysRevB.51.14370.

[72] K. Tanaka, T. Takahashi, T. Kondo, T. Umebayashi, K. Asai, K. Ema, Image charge effect on two-dimensional excitons in an inorganic–organic quantum-well crystal, Phys. Rev. B 71 (2005) 045312, https://doi.org/10.1103/PhysRevB.71.045312.

[73] C.C. Stoumpos, D.H. Cao, D.J. Clark, J. Young, J.M. Rondinelli, J.I. Jang, J.T. Hupp, M.G. Kanatzidis, Ruddlesden–Popper hybrid lead iodide perovskite 2D homologous semiconductors, Chem. Mater. 28 (2016) 2852–2867, https://doi.org/10.1021/acs.chemmater.6b00847.

[74] K. Tanaka, T. Kondo, Bandgap and exciton binding energies in lead-iodide-based natural quantum-well crystals, Sci. Technol. Adv. Mater. 4 (2003) 599–604, https://doi.org/10.1016/j.stam.2003.09.019.

[75] C.C. Stoumpos, C.M.M. Soe, H. Tsai, W. Nie, J.-C. Blancon, D.H. Cao, F. Liu, B. Traoré, C. Katan, J. Even, A.D. Mohite, M.G. Kanatzidis, High members of the 2D Ruddlesden–Popper halide perovskites: synthesis, optical properties, and solar cells of (CH3(CH2)3NH3)2(CH3NH3)4Pb5I16, Chem 2 (2017) 427–440, https://doi.org/10.1016/j.chempr.2017.02.004.

[76] M.D. Smith, E.J. Crace, A. Jaffe, H.I. Karunadasa, The diversity of layered halide perovskites, Annu. Rev. Mater. Res. 48 (2018) 111–136, https://doi.org/10.1146/annurev-matsci-070317-124406.

[77] M.D. Smith, L. Pedesseau, M. Kepenekian, I.C. Smith, C. Katan, J. Even, H.I. Karunadasa, Decreasing the electronic confinement in layered perovskites through intercalation, Chem. Sci. 8 (2017) 1960–1968, https://doi.org/10.1039/C6SC02848A.

[78] M.D. Smith, H.I. Karunadasa, White-light emission from layered halide perovskites, Acc. Chem. Res. 51 (2018) 619–627, https://doi.org/10.1021/acs.accounts.7b00433.

[79] M. Fox, Optical Properties of Solids, Oxford University Press, Oxford, 2001.

[80] Z. Yuan, Y. Shu, Y. Tian, Y. Xin, B. Ma, A facile one-pot synthesis of deep blue luminescent lead bromide perovskite microdisks, Chem. Commun. 51 (2015) 16385–16388, https://doi.org/10.1039/C5CC06750B.

[81] Y. Tong, F. Ehrat, W. Vanderlinden, C. Cardenas-Daw, J.K. Stolarczyk, L. Polavarapu, A.S. Urban, Dilution-induced formation of hybrid perovskite nanoplatelets, ACS Nano 10 (2016) 10936–10944, https://doi.org/10.1021/acsnano.6b05649.

[82] J.-C. Blancon, A. Stier, H. Tsai, W. Nie, C. Stoumpos, B. Traoré, L. Pedesseau, M. Kepenekian, F. Katsutani, G. Noe, J. Kono, S. Tretiak, S. Crooker, C. Katan, M.G. Kanatzidis, J.J. Crochet, J.M. Even, A.D. Mohite, Scaling law for excitons in 2D perovskite quantum wells, Nat. Commun. 9 (2018) 2254, https://doi.org/10.1038/s41467-018-04659-x.

[83] G. Lanty, K. Jemli, Y. Wei, J. Leymarie, J. Even, J.-S. Lauret, E. Deleporte, Room-temperature optical tunability and inhomogeneous broadening in 2D-layered organic–inorganic perovskite pseudobinary alloys, J. Phys. Chem. Lett. 5 (2014) 3958–3963, https://doi.org/10.1021/jz502086e.

[84] M.C. Weidman, M. Seitz, S.D. Stranks, W.A. Tisdale, Highly tunable colloidal perovskite nanoplatelets through variable cation, metal, and halide composition, ACS Nano 10 (2016) 7830–7839, https://doi.org/10.1021/acsnano.6b03496.

[85] P. Li, B. Shivananju, Y. Zhang, S. Li, Q. Bao, High performance photodetector based on 2D CH3NH3PbI3 perovskite nanosheets, J. Phys. D Appl. Phys. 50 (2017) 094002, https://doi.org/10.1088/1361-6463/aa5623.

[86] J. Zhou, Y. Chu, J. Huang, Photodetectors based on two-dimensional layer-structured hybrid lead iodide perovskite semiconductors, ACS Appl. Mater. Interf. 8 (2016) 25660–25666, https://doi.org/10.1021/acsami.6b09489.

[87] R. Dong, C. Lan, X. Xu, X. Liang, X. Hu, D. Li, Z. Zhou, L. Shu, S. Yip, C. Li, S.-W. Tsang, J.C. Ho, Novel series of quasi-2D Ruddlesden–Popper perovskites based on short-chained spacer cation for enhanced photodetection, ACS Appl. Mater. Interf. 10 (2018) 19019–19026, https://doi.org/10.1021/acsami.8b03517.

[88] Z. Tan, Y. Wu, H. Hong, J. Yin, J. Zhang, L. Lin, M. Wang, X. Sun, L. Sun, Y. Huang, K. Liu, Z. Liu, H. Peng, Two-dimensional (C4H9NH3)2PbBr4 perovskite crystals for high-performance photodetector, J. Am. Chem. Soc. 138 (2016) 16612–16615, https://doi.org/10.1021/jacs.6b11683.

[89] D. Yu, F. Cao, Y. Shen, X. Liu, Y. Zhu, H. Zeng, Dimensionality and interface engineering of 2D homologous perovskites for boosted charge-carrier transport and photodetection performances, J. Phys. Chem. Lett. 8 (2017) 2565–2572, https://doi.org/10.1021/acs.jpclett.7b00993.

[90] X. Liu, D. Yu, F. Cao, X. Li, J. Ji, J. Chen, X. Song, H. Zeng, Low-voltage photodetectors with high responsivity based on solution-processed micrometer-scale all-inorganic perovskite nanoplatelets, Small 13 (2017) 1700364, https://doi.org/10.1002/smll.201700364.

[91] X. Li, D. Yu, J. Chen, Y. Wang, F. Cao, Y. Wei, Y. Wu, L. Wang, Y. Zhu, Z. Sun, J. Ji, Y. Shen, H. Sun, H. Zeng, Constructing fast carrier tracks into flexible perovskite photodetectors to greatly improve responsivity, ACS Nano 11 (2017) 2015–2023, https://doi.org/10.1021/acsnano.6b08194.

[92] M. Era, S. Morimoto, T. Tsutsui, S. Saito, Organic-inorganic heterostructure electroluminescent device using a layered perovskite semiconductor (C6H5C2H4NH3)2PbI4, Appl. Phys. Lett. 65 (1994) 676–678, https://doi.org/10.1063/1.112265.

[93] T. Hattori, T. Taira, M. Era, T. Tsutsui, S. Saito, Highly efficient electroluminescence from a heterostructure device combined with emissive layered-perovskite and an electron-transporting organic compound, Chem. Phys. Lett. 254 (1996) 103–108, https://doi.org/10.1016/0009-2614(96)00310-7.

[94] D. Liang, Y. Peng, Y. Fu, M.J. Shearer, J. Zhang, J. Zhai, Y. Zhang, R.J. Hamers, T.L. Andrew, S. Jin, Color-pure violet-light-emitting diodes based on layered

lead halide perovskite nanoplates, ACS Nano 10 (2016) 6897–6904, https://doi.org/10.1021/acsnano.6b02683.

[95] R. Li, C. Yi, R. Ge, W. Zou, L. Cheng, N. Wang, J. Wang, W. Huang, Room-temperature electroluminescence from two-dimensional lead halide perovskites, Appl. Phys. Lett. 109 (2016) 151101, https://doi.org/10.1063/1.4964413.

[96] L. Ni, U. Huynh, A. Cheminal, T.H. Thomas, R. Shivanna, T.F. Hinrichsen, S. Ahmad, A. Sadhanala, A. Rao, Real-time observation of exciton−phonon coupling dynamics in self-assembled hybrid perovskite quantum wells, ACS Nano 11 (2017) 10834–10843, https://doi.org/10.1021/acsnano.7b03984.

[97] M. Yuan, L.N. Quan, R. Comin, G. Walters, R. Sabatini, O. Voznyy, S. Hoogland, Y. Zhao, E.M. Beauregard, P. Kanjanaboos, Z. Lu, D.H. Kim, E.H. Sargent, Perovskite energy funnels for efficient light-emitting diodes, Nat. Nano-technol. 11 (2016) 872–877, https://doi.org/10.1038/nnano.2016.110.

[98] J. Byun, H. Cho, C. Wolf, M. Jang, A. Sadhanala, R.H. Friend, H. Yang, T.W. Lee, Efficient visible quasi-2D perovskite light-emitting diodes, Adv. Mater. 28 (2016) 7515–7520, https://doi.org/10.1002/adma.201601369.

[99] N. Wang, L. Cheng, R. Ge, S. Zhang, Y. Miao, W. Zou, C. Yi, Y. Sun, Y. Cao, R. Yang, Y. Wei, Q. Guo, Y. Ke, M. Yu, Y. Jin, Y. Liu, Q. Ding, D. Di, L. Yang, G. Xing, H. Tian, C. Jin, F. Gao, R.H. Friend, J. Wang, W. Huang, Perovskite light-emitting diodes based on solution-processed self-organized multiple quantum wells, Nat. Photonics 10 (2016) 699–704, https://doi.org/10.1038/nphoton.2016.185.

[100] Z. Xiao, R.A. Kerner, L. Zhao, N.L. Tran, K.M. Lee, T.-W. Koh, G.D. Scholes, B.P. Rand, Efficient perovskite light-emitting diodes featuring nanometre-sized crystallites, Nat. Photonics 11 (2017) 108–115, https://doi.org/10.1038/nphoton.2016.269.

[101] X. Yang, X. Zhang, J. Deng, Z. Chu, Q. Jiang, J. Meng, P. Wang, L. Zhang, Z. Yin, J. You, Efficient green light-emitting diodes based on quasi-two-dimensional composition and phase engineered perovskite with surface passivation, Nat. Commun. 9 (2018) 570, https://doi.org/10.1038/s41467-018-02978-7.

[102] M. Wei, W. Sun, Y. Liu, Z. Liu, L. Xiao, Z. Bian, Z. Chen, Highly luminescent and stable layered perovskite as the emitter for light emitting diodes, Phys. Status Solidi A 213 (2016) 2727–2732, https://doi.org/10.1002/pssa.201600246.

[103] D.N. Congreve, M.C. Weidman, M. Seitz, W. Paritmongkol, N.S. Dahod, W.A. Tisdale, Tunable light-emitting diodes utilizing quantum-confined layered perovskite emitters, ACS Photonics 4 (2017) 476–481, https://doi.org/10.1021/acsphotonics.6b00963.

[104] L.N. Quan, Y. Zhao, F.P. García de Arquer, R. Sabatini, G. Walters, O. Voznyy, R. Comin, Y. Li, J.Z. Fan, H. Tan, J. Pan, M. Yuan, O.M. Bakr, Z. Lu, D.H. Kim, E.H. Sargent, Tailoring the energy landscape in quasi-2D halide perovskites enables efficient green-light emission, Nano Lett. 17 (2017) 3701–3709, https://doi.org/10.1021/acs.nanolett.7b00976.

[105] Y. Ling, Z. Yuan, Y. Tian, X. Wang, J.C. Wang, Y. Xin, K. Hanson, B. Ma, H. Gao, Bright light-emitting diodes based on organometal halide perovskite nano-platelets, Adv. Mater. 28 (2016) 305–311, https://doi.org/10.1002/adma.201503954.

[106] S. Kumar, J. Jagielski, S. Yakunin, P. Rice, Y.-C. Chiu, M. Wang, G. Nedelcu, Y. Kim, S. Lin, E.J. Santos, M.V. Kovalenko, C.-J. Shih, Efficient blue electroluminescence using quantum-confined two-dimensional perovskites, ACS Nano 10 (2016) 9720–9729, https://doi.org/10.1021/acsnano.6b05775.

[107] J. Si, Y. Liu, Z. He, H. Du, K. Du, D. Chen, J. Li, M. Xu, H. Tian, H. He, D. Di, C. Lin, Y. Cheng, J. Wang, Y. Jin, Efficient and high-color-purity light-emitting diodes based on in situ grown films of CsPbX₃ (X = Br, I) nanoplates with controlled thicknesses, ACS Nano 11 (2017) 11100–11107, https://doi.org/10.1021/acsnano.7b05191.

[108] S. Zhang, C. Yi, N. Wang, Y. Sun, W. Zou, Y. Wei, Y. Cao, Y. Miao, R. Li, Y. Yin, N. Zhao, J. Wang, W. Huang, Efficient red perovskite light-emitting diodes based on solution-processed multiple quantum wells, Adv. Mater. 29 (2017) 1606600, https://doi.org/10.1002/adma.201606600.

[109] J. Chang, S. Zhang, N. Wang, Y. Sun, Y. Wei, R. Li, C. Yi, J. Wang, W. Huang, Enhanced performance of red perovskite light-emitting diodes through the dimensional tailoring of perovskite multiple quantum wells, J. Phys. Chem. Lett. 9 (2018) 881–886, https://doi.org/10.1021/acs.jpclett.7b03417.

[110] M. Yang, N. Wang, S. Zhang, W. Zou, Y. He, Y. Wei, M. Xu, J. Wang, W. Huang, Reduced efficiency roll-off and enhanced stability in perovskite light-emitting diodes with multiple quantum wells, J. Phys. Chem. Lett. 9 (2018) 2038–2042, https://doi.org/10.1021/acs.jpclett.8b00600.

[111] Y. Tian, C. Zhou, M. Worku, X. Wang, Y. Ling, H. Gao, Y. Zhou, Y. Miao, J. Guan, B. Ma, Highly efficient spectrally stable red perovskite light-emitting diodes, Adv. Mater. 30 (2018) 1707093, https://doi.org/10.1002/adma.201707093.

[112] M.A. Green, A. Ho-Baillie, H.J. Snaith, The emergence of perovskite solar cells, Nat. Photonics 8 (2014) 506–514, https://doi.org/10.1038/nphoton.2014.134.

[113] S.D. Stranks, H.J. Snaith, Metal-halide perovskites for photovoltaic and light-emitting devices, Nat. Nanotechnol. 10 (2015) 391–402, https://doi.org/10.1038/nnano.2015.90.

[114] M. Li, C. Zhao, Z.K. Wang, C.C. Zhang, H.K. Lee, A. Pockett, J. Barbé, W.C. Tsoi, Y.G. Yang, M.J. Carnie, X.-Y. Gao, W.-X. Yang, J.R. Durrant, L.-S. Liao, S.M. Jain, Interface modification by ionic liquid: a promising candidate for indoor light harvesting and stability improvement of planar perovskite solar cells, Adv. Energy Mater. 8 (2018) 1801509, https://doi.org/10.1002/aenm.201801509.

[115] Z.K. Wang, L.S. Liao, Doped charge-transporting layers in planar perovskite solar cells, Adv. Opt. Mater. 6 (2018) 1800276, https://doi.org/10.1002/adom.201800276.

[116] Y. Yang, J. You, Make perovskite solar cells stable, Nature 544 (2017) 155–156, https://doi.org/10.1038/544155a.

[117] I.C. Smith, E.T. Hoke, D. Solis-lbarra, M.D. McGehee, H.I. Karunadasa, A layered hybrid perovskite solar-cell absorber with enhanced moisture stability, Angew. Chem. 126 (2014) 11414–11417, https://doi.org/10.1002/ange.201406466.

[118] D.H. Cao, C.C. Stoumpos, O.K. Farha, J.T. Hupp, M.G. Kanatzidis, 2D homologous perovskites as light-absorbing materials for solar cell applications, J. Am. Chem. Soc. 137 (2015) 7843–7850, https://doi.org/10.1021/jacs.5b03796.

[119] H. Tsai, W. Nie, J.-C. Blancon, C.C. Stoumpos, R. Asadpour, B. Harutyunyan, A.J. Neukirch, R. Verduzco, J.J. Crochet, S. Tretiak, L. Pedesseau, J. Even, M.A. Alam, G. Gupta, J. Lou, P.M. Ajayan, M.J. Bedzyk, M.G. Kanatzidis, A.D. Mohite, High-efficiency two-dimensional Ruddlesden−Popper perovskite solar cells, Nature 536 (2016) 312–316, https://doi.org/10.1038/nature18306.

[120] X. Zhang, X. Ren, B. Liu, R. Munir, X. Zhu, D. Yang, J. Li, Y. Liu, D.-M. Smilgies, R. Li, Z. Yang, T. Niu, X. Wang, A. Amassian, K. Zhao, S. Liu, Stable high efficiency two-dimensional perovskite solar cells via cesium doping, Energy Environ. Sci. 10 (2017) 2095–2102, https://doi.org/10.1039/C7EE01145H.

[121] N. Zhou, Y. Shen, L. Li, S. Tan, N. Liu, G. Zheng, Q. Chen, H. Zhou, The exploration of crystallization kinetics in quasi two-dimensional perovskite and high performance solar cells, J. Am. Chem. Soc. 140 (2018) 459–465, https://doi.org/10.1021/jacs.7b11157.

[122] Y. Chen, Y. Sun, J. Peng, W. Zhang, X. Su, K. Zheng, T. Pullerits, Z. Liang, Tailoring organic cation of 2D air-stable organometal halide perovskites for highly efficient planar solar cells, Adv. Energy Mater. 7 (2017) 1700162, https://doi.org/10.1002/aenm.201700162.

[123] R.L. Milot, R.J. Sutton, G.E. Eperon, A.A. Haghighirad, J. Martinez Hardigree, L. Miranda, H.J. Snaith, M.B. Johnston, L.M. Herz, Charge-carrier dynamics in 2D hybrid metal−halide perovskites, Nano Lett. 16 (2016) 7001–7007, https://doi.org/10.1021/acs.nanolett.6b03114.

[124] X. Wu, M.T. Trinh, X.-Y. Zhu, Excitonic many−body interactions in two-dimensional lead iodide perovskite quantum wells, J. Phys. Chem. C 119 (2015) 14714–14721, https://doi.org/10.1021/acs.jpcc.5b00148.

[125] K. Tanaka, T. Takahashi, T. Kondo, K. Umeda, K. Ema, T. Umebayashi, K. Asai, K. Uchida, N. Miura, Electronic and excitonic structures of inorganic−organic perovskite-type quantum-well crystal (C₄H₉NH₃)₂PbBr₄, Jpn. J. Appl. Phys. 44 (2005) 5923–5932, https://doi.org/10.1143/JJAP.44.5923.

[126] Z. Cheng, J. Lin, Layered organic−inorganic hybrid perovskites: structure, optical properties, film preparation, patterning and templating engineering, CrystEngComm 12 (2010) 2646–2662, https://doi.org/10.1039/C001929A.

[127] K. Yao, X. Wang, Y.-X. Xu, F. Li, L. Zhou, Multilayered perovskite materials based on polymeric-ammonium cations for stable large-area solar cell, Chem. Mater. 28 (2016) 3131–3138, https://doi.org/10.1021/acs.chemmater.6b00711.

[128] L.N. Quan, M. Yuan, R. Comin, O. Voznyy, E.M. Beauregard, S. Hoogland, A. Buin, A.R. Kirmani, K. Zhao, A. Amassian, D.H. Kim, E.H. Sargent, Ligand-stabilized reduced-dimensionality perovskites, J. Am. Chem. Soc. 138 (2016) 2649–2655, https://doi.org/10.1021/jacs.5b11740.

[129] J. Liu, J. Leng, K. Wu, J. Zhang, S. Jin, Observation of internal photoinduced electron and hole separation in hybrid two-dimensional perovskite films, J. Am. Chem. Soc. 139 (2017) 1432–1435, https://doi.org/10.1021/jacs.6b12581.

[130] J. Qing, X.K. Liu, M. Li, F. Liu, Z. Yuan, E. Tiukalova, Z. Yan, M. Duchamp, S. Chen, Y. Wang, S. Bai, J.-M. Liu, H.J. Snaith, C.-S. Lee, T.C. Sum, F. Gao, Aligned and graded type-II Ruddlesden−Popper perovskite films for efficient solar cells, Adv. Energy Mater. 8 (2018) 1800185, https://doi.org/10.1002/aenm.201800185.

[131] Y. Hu, J. Schlipf, M. Wussler, M.L. Petrus, W. Jaegermann, T. Bein, P. Müller-Buschbaum, P. Docampo, Hybrid perovskite/perovskite heterojunction solar cells, ACS Nano 10 (2016) 5999–6007, https://doi.org/10.1021/acsnano.6b01535.

[132] T.M. Koh, J. Huang, I. Neogi, P.P. Boix, S.G. Mhaisalkar, N. Mathews, High stability bilayered perovskites through crystallization driven self-assembly, ACS Appl. Mater. Interf. 9 (2017) 28743–28749, https://doi.org/10.1021/acsami.7b07780.

[133] G. Grancini, C. Roldán-Carmona, I. Zimmermann, E. Mosconi, X. Lee, D. Martineau, S. Narbey, F. Oswald, F. De Angelis, M. Graetzel, M.K. Nazeeruddin, One-year stable perovskite solar cells by 2D/3D interface engineering, Nat. Commun. 8 (2017) 15684, https://doi.org/10.1038/ncomms15684.

[134] M.H. Li, H.H. Yeh, Y.H. Chiang, U.S. Jeng, C.J. Su, H.W. Shiu, Y.J. Hsu, N. Kosugi, T. Ohigashi, Y.A. Chen, P.-S. Shen, P. Chen, T.-F. Guo, Highly efficient 2D/3D hybrid perovskite solar cells via low-pressure vapor-assisted solution process, Adv. Mater. 30 (2018) 1801401, https://doi.org/10.1002/adma.201801401.

[135] Z. Wang, Q. Lin, F.P. Chmiel, N. Sakai, L.M. Herz, H.J. Snaith, Efficient ambient-air-stable solar cells with 2D−3D heterostructured butylammonium-caesium-formamidinium lead halide perovskites, Nat. Energy 2 (2017) 17135, https://doi.org/10.1038/nenergy.2017.135.

[136] A. Abate, Perovskite solar cells go lead free, Joule 1 (2017) 659–664, https://doi.org/10.1016/j.joule.2017.09.007.

[137] M. Konstantakou, T. Stergiopoulos, A critical review on tin halide perovskite solar cells, J. Mater. Chem. A 5 (2017) 11518–11549, https://doi.org/10.1039/C7TA00929A.

[138] M. Li, Z.K. Wang, M.P. Zhuo, Y. Hu, K.H. Hu, Q.Q. Ye, S.M. Jain, Y.G. Yang, X.Y. Gao, L.S. Liao, Pb−Sn−Cu ternary organometallic halide perovskite solar

cells, Adv. Mater. 30 (2018) 1800258, https://doi.org/10.1002/adma.201800258.

[139] D.B. Mitzi, C. Feild, W. Harrison, A. Guloy, Conducting tin halides with a layered organic-based perovskite structure, Nature 369 (1994) 467, https://doi.org/10.1038/369467a0.

[140] C. Kagan, D. Mitzi, C. Dimitrakopoulos, Organic–inorganic hybrid materials as semiconducting channels in thin-film field-effect transistors, Science 286 (1999) 945–947, https://doi.org/10.1126/science.286.5441.945.

[141] Y. Liao, H. Liu, W. Zhou, D. Yang, Y. Shang, Z. Shi, B. Li, X. Jiang, L. Zhang, L.N. Quan, R. Quintero-Bermudez, B.R. Sutherland, Q. Mi, E.H. Sargent, Z. Ning, Highly oriented low-dimensional tin halide perovskites with enhanced stability and photovoltaic performance, J. Am. Chem. Soc. 139 (2017) 6693–6699, https://doi.org/10.1021/jacs.7b01815.

[142] D.H. Cao, C.C. Stoumpos, T. Yokoyama, J.L. Logsdon, T.-B. Song, O.K. Farha, M.R. Wasielewski, J.T. Hupp, M.G. Kanatzidis, Thin films and solar cells based on semiconducting two-dimensional Ruddlesden–Popper $(CH_3(CH_2)_3NH_3)_2(CH_3NH_3)_{n-1}Sn_nI_{3n+1}$ perovskites, ACS Energy Lett. 2 (2017) 982–990, https://doi.org/10.1021/acsenergylett.7b00202.

[143] S. Shao, J. Liu, G. Portale, H.H. Fang, G.R. Blake, G.H. ten Brink, L.J.A. Koster, M.A. Loi, Highly reproducible Sn-based hybrid perovskite solar cells with 9% efficiency, Adv. Energy Mater. 8 (2018) 1702019, https://doi.org/10.1002/aenm.201702019.

[144] C. Ran, J. Xi, W. Gao, F. Yuan, T. Lei, B. Jiao, X. Hou, Z. Wu, Bilateral interface engineering toward efficient 2D–3D bulk heterojunction tin halide lead-free perovskite solar cells, ACS Energy Lett. 3 (2018) 713–721, https://doi.org/10.1021/acsenergylett.8b00085.

[145] R. Quintero-Bermudez, A. Gold-Parker, A.H. Proppe, R. Munir, Z. Yang, S.O. Kelley, A. Amassian, M.F. Toney, E.H. Sargent, Compositional and orientational control in metal halide perovskites of reduced dimensionality, Nat. Mater. 17 (2018) 900–907, https://doi.org/10.1038/s41563-018-0154-x.

[146] S. Wang, L. Lin, Z.L. Wang, Triboelectric nanogenerators as self-powered active sensors, Nano Energy 11 (2015) 436–462, https://doi.org/10.1016/j.nanoen.2014.10.034.

[147] S.F. Leung, K.T. Ho, P.K. Kung, V.K. Hsiao, H.N. Alshareef, Z.L. Wang, J.H. He, A self-powered and flexible organometallic halide perovskite photodetector with very high detectivity, Adv. Mater. 30 (2018) 1704611, https://doi.org/10.1002/adma.201704611.

[148] Y. Zhou, L. You, S. Wang, Z. Ku, H. Fan, D. Schmidt, A. Rusydi, L. Chang, L. Wang, P. Ren, Giant photostriction in organic–inorganic lead halide perovskites, Nat. Commun. 7 (2016) 11193, https://doi.org/10.1038/ncomms11193.

[149] T.C. Wei, H.P. Wang, T.Y. Li, C.H. Lin, Y.H. Hsieh, Y.H. Chu, J.H. He, Photostriction of $CH_3NH_3PbBr_3$ perovskite crystals, Adv. Mater. 29 (2017) 1701789, https://doi.org/10.1002/adma.201701789.

[150] P. Li, Y. Chen, T. Yang, Z. Wang, H. Lin, Y. Xu, L. Li, H. Mu, B.N. Shivananju, Y. Zhang, Two-dimensional $CH_3NH_3PbI_3$ perovskite nanosheets for ultrafast pulsed fiber lasers, ACS Appl. Mater. Interf. 9 (2017) 12759–12765, https://doi.org/10.1021/acsami.7b01709.